Title

Graded mesoderm assembly governs cell fate and morphogenesis of the early mammalian heart.

Permalink

https://escholarship.org/uc/item/40x5s75d

Journal

Cell, 186(3)

Authors

Dominguez, Martin

Krup, Alexis

Muncie, Jonathon

et al.

Publication Date

2023-02-02

DOI

10.1016/j.cell.2023.01.001

Graded mesoderm assembly governs cell fate and morphogenesis of the early mammalian heart

Martin H. Dominguez[1,2,3,7], **Alexis Leigh Krup**[1,4], **Jonathon M. Muncie**[1], **Benoit G. Bruneau**[1,5,6,7,8]

[1.]Gladstone Institutes, San Francisco, CA, USA

[2.]Department of Medicine, Division of Cardiology, University of California, San Francisco, CA, USA

[3.]Cardiovascular Institute, University of Pennsylvania, Philadelphia, PA, USA

[4.]Biomedical Sciences Graduate Program, University of California, San Francisco, CA, USA

[5.]Roddenberry Center for Stem Cell Biology and Medicine at Gladstone, San Francisco, CA, USA

[6.]Department of Pediatrics, Cardiovascular Research Institute, Institute for Human Genetics, and Eli and Edythe Broad Center of Regeneration Medicine and Stem Cell Research, University of California, San Francisco, CA 94158, USA

Summary

Using four-dimensional whole-embryo light sheet imaging with improved and accessible computational tools, we longitudinally reconstruct early murine cardiac development at single-cell resolution. Nascent mesoderm progenitors form opposing density and motility gradients, converting the temporal birth sequence of gastrulation into a spatial anterolateral-to-posteromedial arrangement. Migrating precardiac mesoderm does not strictly preserve cellular neighbor relationships, and spatial patterns only become solidified as the cardiac crescent emerges. Progenitors undergo a mesenchymal-to-epithelial transition, with a first heart field (FHF) ridge apposing a motile juxta-cardiac field (JCF). Anchored along the ridge, the FHF epithelium rotates the JCF forward to form the initial heart tube, along with push-pull morphodynamics of the second heart field. In *Mesp1* mutants that fail to make a cardiac crescent, mesoderm remains highly motile but directionally incoherent, resulting in density gradient inversion. Our practicable live embryo

---

[7.]Corresponding authors: martin.dominguez@pennmedicine.upenn.edu, benoit.bruneau@gladstone.ucsf.edu.
[8.]Lead contact

Declaration of interests

B.G.B. is a founder, shareholder, and advisor of Tenaya Therapeutics, and is an advisor for SilverCreek Pharmaceuticals. The work presented here is not related to the interests of these commercial entities.

imaging approach defines spatial origins and behaviors of cardiac progenitors and identifies their unanticipated morphological transitions.

Graphical Abstract
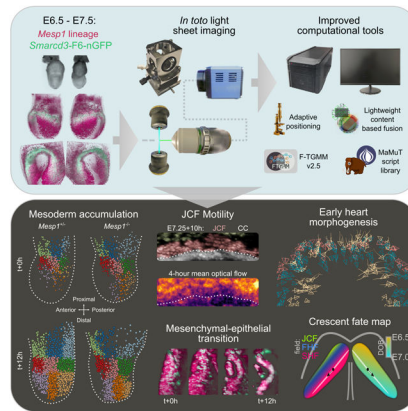
In Brief

Cardiac development is reconstructed at single-cell resolution in live mouse embryos using light sheet imaging and improved computational tools.

Introduction

The emergence and allocation of the progenitors of organs offers insights into the events that ensure robust morphogenesis. The developing heart is particularly sensitive to disturbed morphogenesis, as congenital heart defects (CHDs) occur in over 1% of live births. Understanding the stepwise allocation and assembly of cardiac precursors will provide insights into heart development and disease. Cell labeling and histological studies have shown how the heart forms from its earliest discernible stages,[1–5] but individual cellular events following gastrulation remain mostly uncharacterized.

Cardiovascular progenitors emerge during gastrulation as a subset of the *Mesp1*^{+} nascent mesoderm population, and migrate to lateral regions that will become the cardiac crescent.[6–8] Early cardiac progenitors comprise multipotent progenitor pools, the first and second heart fields (FHF and SHF), as well as a newly-classified juxta-cardiac field (JCF). The JCF contributes to epicardium and left ventricle (LV).[9,10] Partially overlapping the JCF, the FHF contributes to atria, atroventricular canal (AVC) and left ventricle (LV).[6,11] SHF cells contribute to the atria, right ventricle (RV), and outflow tract (OFT).[12,13]

Lineage and clone labeling strategies have revealed that *Mesp1*^{+} progenitors have rudimentary assignments to final cardiac structures (even prior to formation of the heart fields), with either temporal or spatial restriction.[6,7,14] However, unifying evidence between temporal and spatial domains is incomplete, and concretely linking early progenitors to their progeny structures requires examination at greater temporal resolution than lineage tracing alone can afford.

Live imaging of avian cardiogenesis has been insightful, by exploiting the relative accessibility of such embryos for visualization and micro-manipulation.[2,15–17] Imaging studies of early mouse development, however, have grown at a relatively slower pace, owing to the fragility and limited longevity of *ex vivo* embryo culture.[18–21] Recent studies have examined gastrulation[22] and cardiogenesis[23] in the mouse, but were limited to examining only a few cells at a time with confocal microscopy.

Light sheet fluorescence microscopy (LSFM) is well suited to morphogenetic studies of mouse development,[24–27] though most in toto embryo imaging has been performed on highly-specialized, custom-build instruments. While computational analysis of large-scale LSFM data is now possible,[27–30] many existing software applications were designed with the same specialization as the custom microscopes with which they are paired.

Overcoming these roadblocks, we performed comprehensive whole-embryo analyses to examine early cardiac progenitors and their emergence from *Mesp1*⁺ mesoderm. We combined a widely-available LSFM setup and murine *ex vivo* embryo culture (Fig. 1A), integrating data from fluorescent reporters for both *Mesp1* lineage and the *Smarcd3* "F6" enhancer, the latter being the earliest known cardiac-specific identifier.[6] Furthermore, we improved computational tools to enhance data collection, image processing, and analysis of such large-scale data, as well as to help democratize the use of live embryo imaging.

By tracking cardiogenesis at single cell resolution with retrospective *in silico* labeling, our work reveals how cardiac regional fate is intimately tied to the temporal birth and migration sequence of cardiac progenitors. Additionally, we highlight the morphological formation of cardiac epithelium, uncovering region-specific migration and movement behaviors that ultimately shape and sculpt the early heart.

Results

An improved computational workflow for in toto mouse embryogenesis by multi-view LSFM

McDole et al. described a comprehensive, whole-embryo imaging workflow of mouse post-implantation development.[29] The powerful LSFM microscope utilized in that study provides unparalleled imaging, but its complex assembly and upkeep requires dedicated specialists. Alternatively, advanced commercial LSFM setups (now widely available), such as the Zeiss Lightsheet Z.1, performed excellently in auditions with our embryos. However, long imaging runs required minor accommodations, including the development of an adaptive position correction application (ZLAPS) that interfaces with the Zeiss software (Fig. 1A).

We empirically determined that 2–3 specimen views acquired at 6-minute intervals would produce an acceptable balance of data return and phototoxicity, and sought a compatible computational pipeline for downstream analysis. Raw data per experiment can range from 2 to 4 terabytes, depending on number of views, channels, and duration. A true in toto approach then "fuses" those views to form a single comprehensive image volume of the entire specimen, often applying deblurring methods in the process.[31]

One such method, multiview deconvolution, becomes computationally efficient with 4 or more views.[32] As we utilize only 2–3 oblique views of each embryo, we crafted an open-source single-view deconvolution and fusion workflow (Fig. 1B), avoiding iterative methods with staggering processing overhead. Our macro-based application employs closed-form deconvolution[33] in batch (using theoretical PSFs), and offers further enhancement with Fiji's background subtraction algorithm.[34] We next employed BigStitcher[28], a user-friendly tool for registering (i.e. aligning) and fusing (consolidating) multiview LSFM datasets in 4d (Fig. 1C).

Within BigStitcher, we carefully examined content-based fusion, which produces higher quality results than mean fusion (Fig. S1A), by estimating regions of entropy (i.e. noise) in each view to weight the output in favor of entropy-low regions. However, content-based fusion is impractical or even unattainable with large datasets due to its memory and CPU consumption. Since the weight images for each view are, in effect, compacted summaries of the content within the image, we reasoned that downscaling prior to entropy calculation might have little effect on either the weight images or the fusion results. Indeed, 2X or 4X downscaling (prior to entropy calculation) produced nearly identical results across a wide range of datasets, but with markedly decreased CPU time and memory usage (Fig. S1A'–A"). We named the optimized algorithm "lightweight" content-based fusion (Fig. 1C).

After multiple views are consolidated into a single volume for each channel and timepoint, tracking is used to estimate each cell's position in space and time. We started with open source TGMM 2.0,[29] adding several enhancements to tracking accuracy and computational efficiency (Fig. S1B). We first improved TGMM's segmentation by employing a dynamic background subtraction routine, utilizing image features to identify background rather than subtracting static pixel values homogeneously (Fig. S1C–D'). Next, we optimized the main tracking loop to minimize repeat calls to hierarchical segmentation by caching their results. Finally, we re-wrote the division detection machine learning classifier to score combinatorial division trios (mother-daughter-daughter) near each cell birth, choosing the best trio for the final solution (Fig. S1H–I). With its ultimate iteration designated v2.5, Forked Tracking with Gaussian Mixture Models (F-TGMM) represents a stabler and more accurate tracking package (Fig. S1G) that runs 30% faster than TGMM 2.0 (Fig. S1B').

TGMM data can be analyzed as raw tracks (Fig. 1E), which spuriously and stochastically terminate owing to imperfect linkage across time (Fig. S1E–G). Alternatively, tracks can be extended in time to create a morphodynamic overview of the dataset, using a package called statistical vector flow (SVF, Fig. 1E).[29] The open source Fiji plugin, MaMuT, is used for visualization of raw tracks and SVF results.[30] We updated SVF for use with Python 3, and enhanced MaMuT for 3d viewing of large datasets, and for displaying cell vector flow (Fig. 1E). Lastly, we wrote a collection of scripts for MaMuT dataset manipulations (Fig. 1E) such as: selective labeling/coloring of embryo regions/tissues, subsetting and concatenating datasets, exporting track data for statistical analysis, filtering or excluding tracks by cell or track features, and others.

Overall, these computational tools facilitate collection, analysis, and visualization of in toto live imaging data. We applied this comprehensive package to the investigation of

mesoderm migration and early cardiac morphogenesis, though it could be used in a variety of applications. All are open source and portable, and compatible with contemporary hardware and software.

A spatiotemporal gradient of mesoderm accumulation

After finalizing the computational toolbox for live imaging of mouse embryos, we examined behavior during and immediately following gastrulation, as cardiac progenitors are born. Using *Mesp1* lineage reporter mice (see Fig. S2A for details on RCL-H2B-mCherry reporter onset), we began in toto experiments at the E6.5 / mid streak (MS) stage, when only a few progenitors have arrived in the mesoderm layer (Fig. 2A and Video S1). Across all embryos studied, we noticed stereotypical collective migration of the mesoderm, yet stochastic individual cell behaviors.

Generally, *Mesp1* progeny filled the mesoderm layer in an orderly spatiotemporal pattern. Migrating from posterior regions, the nascent progenitors settled first in anterior and proximal locations, followed by progressively posterior and distal locations (Fig. 2B–C). We assigned 9 bins to the final destinations of the cells (after each 12-hour sequence), and analyzed the raw tracks for cell density, motility, and birthdate (Fig. 2B'). This showed that cells migrating within the posterior-distal locations were less dense, more motile, and born later than cells in anterior-proximal locations. In flat disc embryos such as those of most amniotes, this would be akin to an anterolateral-to-posteromedial sequence of mesoderm filling, guided by a concomitant density gradient.

SVF-processed tracks also demonstrated similar opposing gradients of birthdate and velocity (Fig. 2C). Quantitative analysis showed that extraembryonic mesoderm cells migrated more slowly than embryonic mesoderm cells (Fig. 2C'), consistent with prior findings.[22] However, as embryonic cells arrived in their positions and the mesoderm layer filled, they slowed to a velocity comparable to that of extraembryonic cells (Fig. 2C').

Holistically, this process creates a dense pileup of slowing cells in anterior and proximal regions, juxtaposed with fast-moving sparser cells in distal and posterior regions that are still accumulating at their destinations. Thus, the embryo grows by posterior and distal extension (Fig. 2E, S2C–D), similar to a traffic jam propagating along a highway, further and further from its origin. E6.75 / late streak (LS) embryos exhibited similar opposing gradients of motility and density (Fig. S2E–G'), as nascent mesoderm is still being born at this stage. However, after E7.0 / early bud stage (EB), few new cells appear, and embryos undergo ventral deformation and head folding (Fig. S2F).

Although the filling of mesoderm was orderly and stereotypical, we noticed that individual cell movements were quite chaotic during migration. Globally, gene expression and cell fate are patterned within the posterior epiblast and primitive streak,[14,35] such that mesoderm and endoderm progenitors arise from distinct molecular and spatiotemporal regions. To subordinate the diverse *Mesp1*+ lineage to even more granular early assignments would likely require progenitors to migrate with mostly linear motion to preserve cell neighbor relationships and therefore pre-ordained spatial information.[14,22] However, our findings

advocate for a more restrained interpretation that full specification may not predate gastrulation, given the considerable cell mixing we observed.

Having manually tracked a large cohort of dividing cells during mesoderm assembly, we studied the migratory patterns of division daughter cells (Fig. 2F, S2K), which necessarily share an ancestral site of origin in the primitive streak. To our surprise, daughter cells underwent substantial separation following division, up to 75μm (or 30% of total embryo length) in two hours (Fig. 2F–G). When mother-daughter and daughter-daughter behavior were compared across stages, the strong separating movements of daughter cells declined as mesoderm assembly proceeded (Fig. 2G). By E7.0 / EB, daughters mostly remained in close proximity.

Similarly, we examined the crossing behavior of migrating cells during gastrulation, by using F-TGMM tracks to determine the extent of mixing of unrelated cells. We observed frequent position swaps of co-migrating cells (Fig. 2H). By summarizing position swaps across two axes in various embryo regions, we again found that tracks cross each another less frequently with incrementing embryo stage (Fig. 2I). Comparing track pairs between E6.5 / MS and E6.75 / LS embryos, we likewise found tighter correlation of start and end positions in older embryos and in proximal (versus distal) locations (Fig. S2I–J').

Collectively, these findings demonstrate that mesoderm assembly occurs in a stereotypical sequence from anterior-proximal to posterior-distal, guided by opposing gradients of density and cell motility. Moreover, considerable cell mixing occurs during this process, evidenced by the lack of preservation of cell neighbor relationships, until gastrulation finishes and positional settlement occurs.

Birth of the *Smarcd3*-F6[+] cardiac progenitors

Next, we examined embryos bearing the *Smarcd3*-F6-nGFP reporter, which utilizes a *cis* enhancer (termed "F6") of BAF complex member *Smarcd3* / Baf60c, that becomes active at E6.75 in cardiac precursors.[6]

We empirically determined that nascent mesoderm at E6.75 / LS could be grossly divided into two compartments on the basis of staining for either MSX1 or FOXC2 (Fig. 3A–B'), representing proximal and extraembryonic versus distal embryonic mesoderm, respectively. These populations likely correspond to distinct "destination cell types" in recent single cell RNAseq analysis of embryos at this stage,[36] though their spatial locales have not been extensively explored. At E6.75 / LS, the earliest *Smarcd3*-F6[+] progenitors were coincidental with the MSX1^{+} population (Fig. 3B–B'), but were distinct from cells expressing FOXC2 (Fig. 3A–A'). Since the *Smarcd3*-F6 lineage populates multiple tissues within all cardiac chambers,[6] we next asked whether the *Smarcd3*-F6[+]/MSX1^{+} population is static or dynamic over time.

After E7.0, when the reporter was sufficiently bright for live imaging, an ongoing increase in *Smarcd3*-F6[+] activity was apparent over the subsequent 12 hours (Fig. 3C, Video S2). However, dramatic ventral folding of the embryo becomes a moving target and obscures expression changes. Lateral mesoderm, especially, underwent greater apparent displacement

than any other region during the sequence (Fig. 3E). We thus employed forward and backward propagation in SVF to mark F6$^+$ tracks at the start (F6$^+$ early cohort) and end (F6$^+$ late cohort) of the sequence, respectively (Fig. 3D). Unexpectedly, we found that a large swath of mesoderm—much larger than the F6$^+$ domain at E6.75—carried a cardiac fate. Thus, the F6$^+$ domain expands distally (i.e. medially) and posteriorly as the reporter turns on, ultimately enveloping the *Smarcd3*-F6$^-$/FOXC2$^+$ domain seen at E6.75 (Fig. 3A). Indeed, the region with late reporter onset actually houses the majority of future cardiac progenitors (Fig. 3D).

A careful review of SVF tracks revealed that the early F6$^+$ cohort had much greater migratory diversity than the late F6$^+$ cohort, the latter of which moved outwardly and anteriorly following the overall expansion and ventral folding of the embryo (Fig. 3F). By contrast, we noted at least three patterns of early F6$^+$ migration, including cells that: 1) migrated into extraembryonic structures; 2) traveled posteriorly within the presumptive JCF space, laying on top of the forming crescent; and 3) followed the forming crescent (similar to the late F6$^+$ cohort) anteriorly. Lastly, we noted that the anterior midline in the mouse was breached around E7.0 / EB by lateral mesoderm bilaterally, and that these incursions across the midline were composed of both early and late F6$^+$ cohorts (Fig. 3G).

When late bud (LB) stage embryos were examined, similar results were obtained (Fig. S3A–E), though the early F6$^+$ cohort had already incorporated more distal and posterior regions by this point. Interestingly, expansion of F6 into more distal regions by E7.25 / early head fold stage (EHF) was paralleled by recession of FOXC2 and onset of ISL1 expression (Fig. S3F–F"). This suggests that distally (i.e. medially), the late F6$^+$ cohort may be associated with SHF fate.

To concretely examine cell fate of the two cohorts, we used *Smarcd3*-F6-CreERT2 mice to lineage label progenitors at timepoints defined by tamoxifen administration. When tamoxifen was given at E5.5 or E6.5, we noted relatively similar contributions to myocardial structures, but with far fewer cells labeled at E5.5 (Fig. 3H–H"), consistent with the known onset of the reporter after E6.5. More interestingly, we noted a shift in the fates of E7.5-labeled cells toward RV and especially outflow structures (Fig. 3H").

While differential temporal fate of cardiac progenitors has been shown previously,[7,14] it is significant here for two reasons. First, the graded onset of the F6 reporter (Fig. 3D) almost perfectly parallels the graded assembly of mesoderm by birthdate (Fig. 2C–E), except that it occurs 6–12 hours later. This parallel is further supported by the strikingly similar results of temporally-labeled *Mesp1* progeny[7] versus F6 progeny (Fig. 3H–H"): early *Mesp1*$^+$ and F6$^+$ cells contribute preferentially to LV, proepicardium, and AVC; late *Mesp1*$^+$ and F6$^+$ cells uniquely contribute to RV, OFT and atria. Second, the positions and marker co-expression of the two F6$^+$ cohorts (as shown here) reveal patterning of the early cardiac crescent: anterolateral MSX1$^+$ cells give rise to LV, proepicardium, and AVC, whereas posteromedial FOXC2$^+$ cells, consistent with their apparent conversion to ISL1 expression (Fig. S3F–F"), contribute to RV and OFT. However, spatially resolving late F6$^+$ regions patterned for OFT or atria requires additional information (or tracking of later stage embryos) because of their contemporaneous birth.

Mesenchymal-epithelial transition of the cardiac crescent

The next steps of cardiogenesis are not well studied in mammals, as tools for labeling the progenitors of interest and for examining their morphogenesis are scarce. Reporter mice such as those based on *Nkx2–5*, for example, initiate visible expression too late (E7.75 / late head fold "LHF," or early somite stages) to capture these phenomena.[23] Therefore, we again took advantage of *Smarcd3*-F6-nGFP reporter embryos undergoing head folding, to understand how the early crescent becomes suitable for forming a closed tube. During and after these stages, many pre-cardiac structures begin to take recognizable form,[23] permitting annotation of cell fates associated with these emerging morphological features (Fig. 4A–B).

At first glance, our observations (Fig. S4A vs. S4B, Video S3) appeared to merely represent mesoderm splitting into splanchnic and somatic layers. However, movements of the F6$^+$ nuclei (4A-A') uncovered several unexpected behaviors. First, the mesoderm simultaneously partitioned into three progeny compartments (Fig. 4A'): prospective endocardium, prospective myocardium, and prospective pericardium (i.e. somatic mesoderm). Second, the process appeared more nuanced than simple trisection of the mesodermal mesenchyme; the prospective myocardium flattened into a continuous single cell layer and expanded outwardly, stretching into the forming foregut pocket (Fig. S4A–B).

We used a whole-cell tdTomato *Mesp1* lineage reporter to quantify the cells' shape and size changes. Consistent with a transformation from dense mesenchyme to planar sheet, cell volume increased, cell density declined, and dorsal-ventral depth of the prospective myocardium decreased (Fig. 4C). Despite the subtle complexity, the morphological changes we observed are reminiscent of a mesenchymal-epithelial transition (MET), a critical morphodynamic step in other developmental processes.[37] Staining of embryos for pan-CADHERIN and α-CATENIN revealed remarkable organization of the peri-membrane compartment in MEF2C$^+$ progenitors undergoing this transition (Fig. 4D–F). Total pan-CADHERIN signal in the cardiac crescent increased (lower chart in Fig. 4G) during this period, and the quantified increase in co-localization of CADHERIN and α-CATENIN (upper chart in Fig. 4G) was more impressive.

To investigate the possible mechanisms for cardiac crescent MET, we analyzed single cell transcriptomes with fine temporal granularity during this process, dating from E7.5 to E8.0 (Fig. 4H–I).[9] We compared *Mef2c*$^+$ cells (to mitigate dissection biases in cell composition) from the two earliest stages, which represent E7.5 / EHF (named "−1") and E7.75 / LHF or early somite (named "0") (Fig. S4E). In scoring gene ontology (GO) biological processes (BP) for membership by differentially-expressed transcripts (Fig. 4J), we noted that the terms "positive regulation of epithelial to mesenchymal (EMT) transition" and "cell-cell junction assembly" were the second- and third-most significant (Fig. 4J). Indeed, numerous EMT-related transcription factors were down-regulated from stage "−1" to stage "0," (Fig. S4F) and a panel of notable members—*Foxc1*, *Twist1*, and *Snai1*—showed clear temporal declines across the entire dataset (Fig. 4K). Conversely, several adherens junction components were up-regulated—*Cdh2*, *Jup*, *Afdn*. Immunostaining corroborated this evidence, revealing an obvious decline in SNAI1 in the center of the cardiac crescent (Fig. 4L), together with increased N-CADHERIN, γ-CATENIN, and N-CADHERIN / γ-CATENIN complexes (Fig. S4H–J).

Movement of cell populations during crescent MET

Because the observed MET occurs coincidentally with reshaping of the cardiac progenitor fields, together with spatial segregation of lineages (FHF, SHF, pericardium, endocardium, etc.), we next asked if we could reconstruct the entire process to determine patterns of cell fate and migration. With annotation guided by time-lapse LSFM footage from *Mef2c*AHF lineage tracing experiments (Figs. 5B–B', S5A–A"), we analyzed 9 tissues by backward propagation of the *Mesp1* lineage in SVF at E7.25 – E7.5 / EHF (Fig. 5A). Interestingly, pericardium and endocardium appeared to originate from progenitors interspersed within the cardiac crescent, yet they were spatially pre-configured within the mesenchyme by dorsal-ventral depth (Fig. 5A'), consistent with the possibility of morphogen transfer between primitive germ layers.[38]

Next, we examined the myocardial fields, which expand considerably as they flatten into a one- or two-cell thick lamina. SVF propagation showed the myocardial fields formed a ventral ridge that extended dorsally into the deepening foregut pocket (Fig. 5C, Video S4), consistent with coordination between myocardium and endoderm.[16] Although the SHF underwent greater movement, its net displacement was lower than either the JCF or FHF when corrected for endoderm deformation (Fig. 5C').

Intriguingly, the JCF showed the greatest corrected SVF displacement of the three heart fields (Fig. 5C'). Moreover, we observed very brisk, seemingly chaotic movements (Fig. 5D and E, Video S4) within the JCF in all of our live experiments. JCF nuclei were more tangentially oriented along the crescent than FHF and SHF (cardiac crescent, "CC") nuclei (Figs. 5D' and S5B–C), and quantifications revealed far greater motility in JCF cells than in the relatively immobile CC (Fig. 5D" and 5E).

To probe transcriptional signatures that could be responsible for this behavior, we examined unique features of the JCF (Figs. 5G–H') in single cell RNAseq datasets (Figs. S5D–E, 5F).[39] In scoring GO BPs for membership by JCF markers (Fig. 5H), we found several significant terms that incorporate motility, adhesion, or migration, and plotted a collection of JCF-enriched member genes (Fig. 5H'). *Nrp1*, a member of three such GO BP terms, was the most unique to the JCF by log2FC, while a number of bone morphogenic protein and other matrix/guidance molecules were not far behind (Fig. 5H').

Transformation of the epithelial cardiac crescent into the early heart tube

Shortly after becoming an epithelium (E7.75 / early somite), cardiac progenitors undergo rapid morphogenesis to form (E8.0) and dorsally close (E8.25) the early heart tube.[23] Using in toto LSFM imaging with TGMM/SVF reconstruction at E7.75 / early somite stage (Fig. 6A–A", Video S5), we observed two notable patterns of movement. First, progenitors within the dorsal aspect of the epithelial sheet lifted off the endocardial surface, causing the ventral-anterior portion of the ridge (along with the overlying JCF) to rotate ('pattern 1', arrowhead in Fig. 6A') by pivoting on the FHF/JCF boundary (which acted as a morphological anchor). The JCF then followed the ventral-directed torsion of the ridge, being dragged and neatly draped around the ventral aspect of the cardiac epithelium. Second, a knob-like

epithelial protrusion propagated posteriorly within the dorsal aspect of the crescent, traveling posteriorly as a wave ('pattern 2', arrowheads in 6A").

SVF reconstructions of this sequence, annotated using time lapse imaging of *Mef2c*AHF lineage tracing experiments (Fig. 5B and S5A–A"), indicated that these two patterns were features of the SHF (Fig. 6B–C). Quantitative tracking showed that SHF cells underwent much greater displacements than either JCF or FHF (Fig. 6C') during this process. Lastly, review of orthogonal SVF projections revealed the anterior- (pattern 1) and medial- (pattern 2) directed motion resulted in opening and closing, respectively, of the early heart tube (Fig. 6D and left panel in 6E). Later, as prospective dorsal mesocardium / dorsal closure myocardium reaches the midline, the patterns converged to drive the epithelial sheet anteriorly into the forming heart (Fig. 6E, right panel).

In fixed embryos labeled with MEF2C^{+} (JCF, FHF, and SHF) and *Mef2c*AHF lineage (SHF only) cells, we found that SHF progenitors entered the forming linear heart tube (LHT) via wave-like translocation or treadmilling of the SHF epithelium through the knob-like structure (Fig. 6F', G', H', arrowheads demarcate FHF boundary, arrows point to dorsal wave). Taken together, these experiments shed light on the diverse morphodynamics of the SHF, both in space and time,[40] indicating that they *concurrently* enact dorsal closure, formation of dorsal mesocardium, and establishment of the arterial pole (see next section).

LHT closure by *Isl1*-dependent morphogenetic wave within differentiating SHF progenitors

Empirical attempts to characterize the SHF epithelial knob-like structure revealed that it was labeled by intermediate expression of ISL1 and NKX2–5 (Fig. S6A–A'''). By single cell RNAseq analysis (Fig. S6B–B'), this zone (intermediate *Isl1* and *Nkx2–5*) resolves to the "Differentiating SHF CMs" cluster, for which a key marker gene was *Tdgf1* (Fig. S6B, C). The unique molecular features of the knob also include extracellular signaling and cytoskeletal factors (Fig S6C–F), for which future investigation may reveal a role in the dramatic morphogenetic behaviors of the knob and related SHF derivatives.

Next, we examined *Nkx2–5* and *Isl1* mutant embryos at E8.5, when dorsal seam myocardium had reached the midline in control LHTs (Fig. S6G", see arrowheads). The comparable region in *Nkx2–5* mutant embryos appeared disorganized, over-folded, and delayed in its approach to the midline (Fig. S6H", see arrowheads). *Isl1* mutants, on the other hand, failed to form a robust knob/wave region (Fig. S6I", see arrowheads), therefore retaining an open configuration of the heart tube, including prospective dorsal mesocardium and aortic sac (Fig. S7C' vs. S7D' and Fig. S6J'" vs. S6K'").

On closer inspection at early somite stages, the SHF was not only present in *Isl1* mutant embryos, but retained its seahorse-like epithelial contour[23] with lower MEF2C expression compared with the FHF (Fig. S7A' versus S7B', see arrowheads). However, *Isl1* mutants exhibited reduced numbers of MEF2C^{+} progenitors (Fig. S7E).

Partially explaining this reduction, we observed decreased proliferation of MEF2C^{+} progenitors in *Isl1* mutants, principally within the morphological SHF (Fig. S7E) as previously reported.[12,41] However, the overall decrease in pHH3[+]/MEF2C^{+} cells was less

than 8% (Fig. S7E), which would require at least 6 division cycles (36 hours at 6 hours/cycle) to confer the 41% reduction in the MEF2C population we noted at these stages (~4530 vs. ~2665, Fig. S7E). Thus, we infer that *Isl1* mutants also exhibit defective cardiac specification, possibly in the form of mis-specification of early *FOXC2*^{+} progenitors to non-cardiac fates (later stage *Isl1* KO embryos demonstrate unusual co-expression of FOXC2 and TNNT2, Fig. S6J" versus S6K").

To uncover additional evidence of aberrant specification, we identified a number of landmark genes along a presumptive vector of SHF differentiation (Fig. S7F), and compared their levels in *Isl1* mutants. A majority of these exhibited decreased expression in microarray experiments derived from cardiac differentiation of *ISL1* KO hESCs,[42] or in RNA sequencing from *Isl1* KO hearts.[43] Especially decreased were genes expressed subsequent to *Isl1* itself (Fig. S7G–H) and implicated in CHDs – such as *Mef2c*, *Nkx2–5*,[44] *Smyd1*,[45] *Ankrd1*.[46] Thus, formation of the early heart requires dynamic SHF morphogenesis instructed by an *Isl1*-dependent program.

Loss of *Mesp1* disrupts the density gradient that forms after gastrulation, altering mesoderm organization

To gain an understanding of cues that control the spatiotemporally-governed early cardiac progenitor behaviors, we studied gastrulation in *Mesp1* mutants, where early organogenesis does not occur due to specification and/or migration defects.[6,8,36,47] Although the movement behaviors of *Mesp1* knockdown cells have been studied *in vitro*,[48] we exploited LSFM and our tracking workflow to better understand their actions *in vivo*.

We observed that the anterior flank of *Mesp1* KO mesoderm did not reach the anterior midline (Figs. 7A–A' versus 7B–B', Video S6). F-TGMM tracks from these LSFM experiments were grouped/binned by their destination position along the anterior-proximal to posterior-distal filling gradient we previously determined (Fig. 7C). Track birthdate and motility gradients were preserved in mutants (Fig. 7C', top and middle panel pairs), but the density gradient appeared flattened and partially inverted (Fig. 7C', bottom panel row). When we examined the spatial vectors of these tracks by binning the gradient into three sections, we observed a severe defect in anterior-directed, as well as outward expansive motion (Fig. 7C"). To explore possible mechanisms for failed directional migration, we analyzed *Mesp1* KO embryos by single cell RNAseq.[49] A host of morphogens, their receptors, and downstream signaling effectors[50] are perturbed in *Mesp1*-null mesoderm progenitors. This includes *Rac1* and *Fgf* genes, which have been shown to be important for directed motility of the mesoderm.[22,50]

Examination of individual tracks in *Mesp1* KO embryos revealed near absence of anterior-directed motion in the anterior, older-born cells (Fig. 7F versus 7E), whereas younger, posterior cells maintained some degree of anterior movement. This abnormal movement of older-born cells may underlie the observed density gradient inversion, as it leads to accumulation of cells in the middle of the embryo rather than antero-proximally (Fig. 7B' vs. 7A'). Directionality, not motility, may thus be the culprit for disorganized *Mesp1* mutant mesoderm.

Discussion

Our improved comprehensive workflow was an important step in overcoming the big data intimidation of LSFM, and aims to simplify and democratize the complexities of live LSFM. Its software components are open source, portable, easier to use than ever before, and the requisite hardware is broadly accessible. Armed with fluorescent reporter mice, a widely available LSFM instrument, and this computational toolbox, we examined a short yet critical and highly dynamic window in mouse development from gestational days 6.5 to 8.0 (Fig. S7I). We identified distinct patterns of mesoderm filling, multipotent cardiac identity, and morphogenesis that critically underlie the emergence of the LHT.

During gastrulation, we observed opposing gradients of progenitor density and motility, similar to the manner in which a traffic jam propagates along the highway further and further from its origin. In presomitic mesoderm of chicks, a random motility gradient controls axis extension,[51,52] and our observations of mouse lateral plate mesoderm are qualitatively and quantitatively similar. Somites, however, are periodic structures, whereas the heart is a singular object formed from the collective migration of precursors to a final destination. Therefore, the motility of lateral mesoderm is unlikely to be completely random, even if it appears quite chaotic. Our examination of *Mesp1* mutants clearly portrays mesoderm movement as directed, since *Mesp1* KO embryos do not form a density gradient and cells lose directionality, thus preventing the completion of mesoderm assembly.

Gastrulating zebrafish embryos are resilient to cell mixing, utilizing morphogenetic gradients to ultimately pattern their mesoderm.[53] Our analysis demonstrates re-arrangement and crossing of cell tracks during gastrulation in the mouse, suggesting that considerable early plasticity must exist among progenitors with respect to final cell fate. Thus, it seems unlikely that rigid fate allocations are present in the primitive streak region before gastrulation, but instead that general trends (i.e. MSX1^{+} vs. FOXC2^{+} nascent mesoderm) are followed with receptivity to patterning cues or landmarks such as those established through morphogen gradients.[54,55]

The distinct spatial patterns of mesoderm assembly and heart field specification, which are oblique to one another (Fig. S7I), likely explain the observed pre-configuration of cardiac fates at the time of gastrulation. As gastrulation terminates, we demonstrate that myocardial progenitors undergo a mesenchymal-epithelial transition (MET) that rapidly extends throughout the entire cardiac crescent, with concurrent changes in EMT and adhesion gene expression, as well as assembly of adherens complexes. From a structure/function perspective, the free-form movement of progenitors, guided by each other and surrounding cues,[50,56] makes for efficient mesoderm filling during gastrulation. However, heart formation requires each cell's movement to act in concert with others (i.e. collective morphogenesis), for which an epithelium is well-suited.

Once the cardiac epithelium is forged, regional discrepancies in morphogenetic behaviors emerge, such as the brisk dance-like movements of the JCF. Our data do not provide a teleological reason for the motility of the JCF. However, it may be that JCF cells are not constrained until the torsional movement of the FHF ridge and push from the SHF

drives them into their pro-epicardial alcove. Besides this anterior 'pushing' behavior that is necessary for opening of the early heart tube, the SHF also exhibits a dramatic wave of differentiation and morphogenesis that propagates posteriorly, forming the heart's dorsal closure and concurrently separating inflow and outflow myocardium. This pull and push mechanism of LHT formation, though unanticipated, explains the complex morphological defects seen in *Isl1* mutants.

Combining these data, we establish a holistic model of early cardiogenesis to unify these findings and reconcile prior evidence (Fig. S5G). Here, the prospective LV (and pro-epicardium) lies at the farthest anterior-lateral extent of the crescent, which is the earliest born during gastrulation. Immediately medial to the LV lies the prospective RV. Within the RV progenitors, the *Tdgf1*+ knob forms as RV and ultimately OFT progenitors are incorporated into the heart. Lateral to the dorsal closure lie the atrial progenitors, which are pulled anteriorly within the epithelial sheet, adding to the venous pole. Still, many unanswered questions remain, such as the necessity and sufficiency of these morphodynamics to heart formation, and the complex molecular events that trigger such dramatic activity.

Overall, our results shed light on an obscure window in early mammalian development, by connecting discrete morphological events in sequence with fine spatial and temporal resolution. This illuminates individual and collective movements of mammalian organ precursors, their origin and dynamic spatial relationships, and the complex and carefully choreographed morphogenetic steps necessary to form an embryonic organ. These findings make an important contribution to cardiac-specific, but likely generalizable features of cell allocation, which may ultimately be identified as broad themes in embryogenesis.

Limitations of the study

Live imaging of mammalian embryogenesis is particularly challenging, as *ex vivo* embryos can diverge from normal development within hours of explantation due to effects of phototoxicity, absence of *in utero* embryotrophic factors, and diffusion-limited supply of nutrients and oxygen. Moreover, computational tracking of cells is imperfect, especially over long durations when linkage inaccuracies compound. Machine-learning and other computational approaches to correctly link division trios are still in their infancy, further limiting lineage reconstruction. We constrained our time-lapse experiments to 9–18 hours to mitigate these factors, which was overall advantageous but nonetheless fragments the developmental sequence. In our analysis, we tempered our expectations for reconstructing complete cell lineages, and avoided automated division detection, instead relying on blinded manual evaluation where cell division information was absolutely essential. Advances in biotechnology, microscopy, and computational analysis will undoubtedly shatter these barriers in years to come.

STAR Methods

Resource Availability

Lead Contact—Further information and requests for resources and reagents should be directed to and will be fulfilled by Benoit G. Bruneau (benoit.bruneau@gladstone.ucsf.edu).

Materials Availability—All unique reagents generated in this study are available from the Lead Contact upon request.

Data and Code Availability

- Live light sheet imaging datasets have been deposited at Image Data Resource (IDR, https://idr.openmicroscopy.org), and are publicly available under accession number idr0146. Repository information is listed in the key resources table. Raw data used for quantification and statistical analysis is deposited at Github (https://github.com/mhdominguez/Dominguez-Cell-2023-DataSources), and is publicly available as of the date of publication.

- All software utilized to handle images, generate and process tracking solutions, and export data tables for analysis are deposited at Github, and are publicly available as of the date of publication. Repositories for each package are listed and linked in the key resources table. Custom R scripts used to perform statistical analysis and to generate individual figure panels are deposited with their accompanying raw data, in the Github repository linked above.

- Any additional information required to reanalyze the data reported in this work paper is available from the Lead Contact upon request.

Experimental Model and Subject Details

Animal Subjects—All mouse protocols were approved by the Institutional Animal Care and Use Committee at UCSF. Mice were housed in a barrier animal facility with standard (12-hour dark/light) husbandry conditions at the Gladstone Institutes. *Smarcd3*-F6-nGFP and *Smarcd3*-F6-CreERT2 mice were described previously.[6] *Mesp1*-Cre knock-in mice[8,47] were obtained from Yumiko Saga. Cre/lox reporter lines RCL-H2B-mCherry and RCL-tdTomato (Ai14) are available at Jackson Laboratory (#023139 and #007914). *Mef2c*AHF-Cre mice were obtained from Brian Black.[57] *Isl1*-Cre and *Nkx2–5*-flox mice are available at Jackson Laboratory (#024242 and #030554). Mice for knockout experiments were maintained on a mixed CD-1 / C57BL/6J background, while control embryos for the majority of live imaging were generated by mating C57BL/6J males to CD-1 females. When indicated in figure panels, multiple reporter and/or mutant alleles may be present in the same embryo(s), either in isolation or in combinations of the following. *Smarcd3*-F6-nGFP refers to $Hipp11^{Smarcd3\text{-}F6\text{-}Hsp68\text{-}nGFP/+}$. "*Smarcd3*-F6 lineage" denotes embryos with $Hipp11^{Smarcd3\text{-}F6\text{-}Hsp68\text{-}CreERT2/+};Rosa26^{CAG\text{-}LSL\text{-}tdTomato/+}$. "*Mesp1* lineage" denotes embryos with $Mesp1^{Cre/+};Rosa26^{CAG\text{-}LSL\text{-}H2BmCherry/+}$ or with $Mesp1^{Cre/+};Rosa26^{CAG\text{-}LSL\text{-}tdTomato/+}$ genotypes. "*Mef2c*AHF lineage" denotes embryos with $Mef2c$AHF-Cre$;Rosa26^{CAG\text{-}LSL\text{-}tdTomato/+}$ genotype. "*Mesp1* KO" or "*Mesp1*$^{-/-}$" are embryos with $Mesp1^{Cre/Cre};Rosa26^{CAG\text{-}LSL\text{-}H2BmCherry/+}$ genotype. "*Isl1* KO" denotes

embryos with $Isl1^{\text{Cre/Cre}}$;$Rosa26^{\text{CAG-LSL-tdTomato/+}}$ genotype, for which matched controls are either $Isl1^{\text{Cre/+}}$;$Rosa26^{\text{CAG-LSL-tdTomato/+}}$ (where $Isl1$ lineage is quantified), or $Isl1^{+/+}$ (where $Isl1$ KO is compared with other mutants). $Nkx2–5$ cKO refers to embryos with $Mesp1^{\text{Cre/+}}$;$Nkx2–5^{\text{flox/flox}}$ genotype, for which matched controls are $Mesp1^{\text{Cre/+}}$;$Nkx2–5^{+/+}$. Following set up of timed matings, the day of copulatory plug is designated as E0.5. For each embryological process we wished to study, we imaged several embryos by time lapse LSFM, though we chose only those with the highest imaging quality for downstream processing and analysis. Gastrulation stages MS to LS: 4 total (2 not processed), cardiac crescent formation EB to EHF: 4 total (1 not processed), EHF to early somite: 6 total (2 not processed), $Mesp1$ KO: 2 total (1 not processed).

Method Details

Whole embryo dissection and culture conditions—Pregnant dams were sacrificed on the day of the experiment, per institutional IACUC standard procedure, and were immediately dissected, with uterus transferred to warm DMEM/F-12 with HEPES and without phenol red. Gestational sacs were transferred to 37°C dissection medium (DMEM/F-12 w/HEPES and w/o phenol red, 10% heat-inactivated fetal bovine serum, 1X penicillin-streptomycin, 1X ITS-X, 1X GlutaMAX, as well as 8 nM β-estradiol, 200 ng/ml progesterone, 25 μM N-acetyl-L-cysteine[58]) in small batches (4–5 per 6cm round bottom dish). While maintaining 37°C as best as possible, embryos were microdissected using fine forceps, and were transferred to 37°C culture medium (identical to dissection medium except with 50% of DMEM/F12 volume replaced by heat-inactivated rat serum, resulting in final 42.5% rat serum) using low-retention wide orifice pipette tips. Embryos were screened for reporter expression and morphology using a standard fluorescence dissection microscope (Leica). Embryo stage was determined with standardized methods,[6] including the use of mouse embryo atlases, in combination with operator judgement for finely granular assessments.

Embryo preparation for live LSFM—Embryos were maintained in culture medium at 37°C and 5% CO_2 until live imaging began. At the time of imaging for embryos at E7.5 and beyond, culture medium was supplemented with 2μM CB-DMB to decrease (but not obliterate) motion artifact from beating due to its activity on Ncx1 channels,[59] for which genetic loss results in normal development with structurally normal hearts until at least E8.5.[60,61] Before mounting, glass capillaries were pre-filled with liquid embedding medium (1.5% agarose, 3% gelatin in PBS, microwaved and mixed until fully melted) and pistons were inserted, then allowed to cool to ~35°C before use. Using a stereoscopic dissection microscope (Leica), each free end (opposite the piston rod) of the embedding mix was extruded and 25–30% of its was length trimmed with a dissection forceps. Each embryo was attached by pushing its ectoplacental cone into the partially-gelled column. After confirming good attachment, the embryo and a small volume of surrounding culture medium were drawn inside the capillary and parked about 4–5mm from the open end. Capillaries containing embryos were maintained at 37°C as best as possible until imaging.

Live LSFM imaging (Fig. 1A)—Lightsheet Z.1 (Zeiss) with incubation and dual pco.edge 4.2 cameras (PCO) was configured prior to embryo harvest, using a 20X/1.0

plan apochromat water-dipping detection objective with refractive index correction collar set to n=1.34–1.35, dual 10X/0.2 illumination objectives, and tank pre-filled with culture medium as described above at 37°C and 5% CO_2. Embryo capillaries were auditioned for imaging quality and position, and chosen embryos subjected to 9–24 hours of LSFM imaging using our Zeiss Lightsheet Adaptive Position System (ZLAPS), linked in the key reagent table. ZLAPS is a user-friendly AutoIT GUI application that interfaces with ZEN, using multiview acquisition settings established by the user. We typically used 2–3 frontal views with 72° - 110° offsets, and collected GFP/488nm/505–545nm and RFP/561nm/570+ nm channels simultaneously. ZLAPS captures new images at fixed time intervals (specified by the user), and calls ImageJ with the Java SIFT[62] plugin to register sequential acquisitions. The registration matrix outputted by SIFT (for each view) is used to adjust (with hysteresis and over-correction mitigation) the stage position of the Z.1 for subsequent acquisitions. For long-term imaging (24hr+), additional optimizations are necessary: light sheet alignment is checked and manually adjusted every 4–6 hours, piston rods are secured with Parafilm, the specimen tank/chamber cover is used, and additional sterile water and/or culture medium is trickled/dripped ($< 0.5mL$/hour) into the tank using a micro-osmotic pump to overcome evaporation losses.

Whole mount preparation for fixed LSFM imaging—Embryos were harvested as for live imaging, except uterus was transported and dissected in ice cold PBS. Embryos were fixed in 4% paraformaldehyde for 1 hour at room temperature with gentle agitation, and washed briefly in PBS before being transferred to short-term storage at 4°C in PBS with 0.2% sodium azide. For immunostaining, embryos were transferred individually to wells of PCR tube strips. E9.5 embryos were cleared briefly in 8% SDS in 200mM sodium borate buffer (pH=8.5),[63] with gentle agitation for a few hours at 37°C until clear, followed by 2–3 washes in PBS at 37°C. Smaller embryos were not subjected to clearing. Subsequently, embryos were incubated in blocking solution (PBS with 5% normal donkey serum, 0.2% sodium azide, and 0.5% TX-100 for E5-E7 embryos, 0.65% for E7-E8, 0.8% for E9) plus 100μg/mL of unconjugated Fab fragment donkey anti-mouse, for 2 hours at 37°C with gentle rocking/rotation. After washing in PBS, primary staining was performed in blocking solution overnight, followed by additional washing. Secondary incubation was performed in blocking solution for 2–3 hours, followed by final washing, with all steps at 37°C with gentle rocking/rotation. For storage at 4°C until mounting, labeled E6-E7 embryos were sunk in 40% glycerol in PBS, while older embryos were kept in PBS.

Fixed LSFM imaging—Embedding medium (2% agarose in PBS) was melted in a microwave and cooled to 35°C, when embryo(s) were immersed for 30 seconds with gentle mixing. Glass capillaries were partially filled with liquid embedding medium, and their pistons were retracted to pick up embryos. Following cooling and gelling of the embedded embryos, capillaries were taped to the inside walls of polystyrene tubes, and specimens were extended into room-temperature immersion medium (EasyIndex OCS for E8+ embryos, or 40% glycerol for E6-E7 embryos) for overnight equilibration. Specimens were imaged on Lightsheet Z.1 (Zeiss) with dual pco.edge 4.2 cameras (PCO) for simultaneous two-channel acquisition using standard illumination lasers (405nm, 488nm, 561nm, 638nm). Rarely, channel bleed necessitated subtraction during processing. Three views were acquired from

the ventral aspect of each specimen at 72° (E7.5+) or 90° (E6.5-E7.25) offsets, using a 20X/1.0 plan apochromat water-dipping detection objective at n=1.38 for 40% glycerol immersion (mated with 10X/0.2 "LSFM" illumination objectives), or a 20X/1.0 plan neofluar clearing dipping objective at n=1.46 for EasyIndex OCS immersion (mated with 10X/0.2 "LSFM clearing" illumination objectives).

Fixed cryosection immunohistochemistry and imaging—After fixing per above, embryos were cryoprotected in 30% sucrose, frozen and sectioned onto slides using a cryostat (14μm sagittal sections). Sections were incubated in primary antibodies in 5% normal donkey serum and 0.2% TX-100 overnight at room temperature, then rinsed three times with PBS before fluorophore-conjugated secondary antibody incubation in PBS. After 2 hours at room temperature, sections were rinsed again and slides were coverslipped in PVA with DABCO. Slides were imaged on an Axio Observer Z1 microscope with Colibri light source and Apotome 3 structured illumination, using a 40X/0.95 plan apochromat air objective (Zeiss).

Computer hardware and software environment—ZEN and Lightsheet Z.1 acquisitions were run on a Zeiss-supplied workstation with dual 8-core 2nd generation Intel Core based Xeon processors and 96GB RAM, running Windows 7. Data was processed on workstations with either single 8-core 10th generation or dual 8-core 3rd generation Intel Core based Xeon CPUs, 128GB RAM, and 4GB Nvidia GTX 1650 GPUs, running Kubuntu 20.04 LTS with Nvidia driver 470, Fiji v2.1.1, Python 3.8.10, Perl 5.30.0, and CUDA toolkit 11.1. All software-comparative benchmarks were run on the same system. Accuracy evaluations between TGMM versions were performed by running each version with its optimized parameter set (determined empirically through iterative comparison), followed by import to MaMuT. Random subsets of cells, tracks, and divisions were assessed in single and double-blinded fashion, with annotations made and counted using MaMuT Perl scripts. Single cell RNAseq analysis was performed on similar hardware running Kubuntu, RStudio desktop build 443, r-base 4.1.3, and Seurat 4.0.6.[64]

Raw image processing and single view deconvolution (Fig. 1B)—ZEN-generated .czi files were handled with our CZI LSFM Processing Scripts (see key resources table) in Fiji.[34] All macros are installed within Fiji, from the source file ("CZI LSFM Processing Macros.ijm"), which lists dependencies/instructions in its header. User-modifiable options are available (macro "Change processing settings…"). The initial step (macros "Deconvolve .czi files") batch processes live or fixed raw data. First, a theoretical point spread function (PSF) is generated, based on illumination and detection parameters (as the intersection of Gaussian light sheet with modeled widefield detection) embedded in Zeiss metadata, with an optional detection NA penalty for the improved aberration handling. Each channel of each view is deconvolved for each timepoint, using a closed form solution with Tikhonov regularization.[33] After .tif files are written for each channel, view, and timepoint, additional automated filtering (macro "Filter LSFM .tif files") is performed that can include (by user option) background subtraction deblurring, bright blob and/or precipitate removal, bit depth compression, z-stack depth equalization (needed for BigStitcher), and/or maximal intensity projection export. Because the many serially-

performed functions have user-controllable settings, changes or alterations to the output images may be somewhat unpredictable *a priori*. For new experiments, a trial-and-error approach is best to determine the optimal workflow. We typically handled fixed image datasets at 16-bit depth with maximal automated filtering including bright blob removal (helpful for deep max Z projections in whole mount IHC), although frequent artifacts remain. Live datasets, on the other hand, were usually contrast-enhanced uniformly across each entire 4d stack, then range-compressed to 8-bit.

Multiview alignment and fusion (Fig. 1C)—After deconvolution and filtering, resultant .tif files were imported into BigStitcher,[28] using its automatic loader. "Interest points" were detected within one or more channels, across all views and timepoints, and views were registered in 3d followed by 4d space. The most optimal solution for live datasets resulted from pre-registration using a "Fast Descriptor-Based" method in 3d then 4d, followed by drift mitigation in time with a "Center-of-mass" method, followed by "Fast Descriptor-Based" or "Precise descriptor-based" methods on the whole dataset and in regions of difficult alignment. Finally, multiple "Iterative closest point" steps were used to improve upon remaining view-to-view (3d) and timepoint-to-timepoint (4th dimension) offsets. Multiview fusion was performed using optimized "lightweight" content-based fusion ("2X" or "4X" downsampling), coded within our fork of BigStitcher's multiview-registration plugin (see key resources table). Other advantages of our forked plugin include fusion in multiple axes, and use of an arbitrary z-anisotropy factor (we use 4 for all datasets). Following fusion into single image volumes (we use h5/xml format, and elect separate files for each timpoint/channel), datasets can be viewed in BigDataViewer in Fiji, or can be further processed in batch using additional components of our CZI LSFM Processing Scripts. This includes automated generation of oblique 3d projections, as well as single-channel anaglyphs (Video S7, using macros "Convert .klb files to anaglyphs or MIPs" or "Convert .tif time series to z-MIP anaglyphs"). Using python, fused .h5 images can be converted to .klb format[29] ("dataset_folder_export_all_h5_to_klb_pyklb-16bit.py"), which is compatible for creating new BigDataViewer datasets (our final dataset format), and for use with F-TGMM.

F-TGMM v2.5—Tracking with Gaussian Mixture Models (TGMM) 1.0,[65] and its successor TGMM 2.0,[29] are open-source packages for analysis of large-scale time-lapse cellular imaging. With linear best-fit modeling (from one timepoint to the next) of a whole-specimen Gaussian mixture, TGMM is fast and accurate. It is written in C++, and utilizes GPU/GPGPU acceleration in CUDA to perform several critical steps. TGMM's accuracy owes itself to several factors: 1. watershed hierarchical segmentation for identifying 3d supervoxels (i.e. Gaussians / prospective cells) – which is superior to a difference-of-gaussians approach as in Trackmate;[66] and 2. the implementation of "temporal logical rules," which build on the linear model by extending false cell deaths, and connecting new births to prospective division parents. We modified TGMM to enhance its performance of with our data. First, over- and under-segmentation were improved by applying dynamic rather than static "background subtraction" to the input images, using Gaussian-blurring (user configurable) to define background. Second, we liberalized the dead cell extension rules to further improve linkage across time. Third, we re-wrote the cell division classifier,

which was constrained to calling 'yes' or 'no' on division trios already assigned by the linear model. Instead, our new classifier incrementally improves division linkage accuracy by sampling trios in the neighborhood of each new birth, and assigning scores to each one. Fourth, we re-wrote the main tracking loop to eliminate repeat calls to hierarchical segmentation for the same image, instead caching the result within the temporal window (usually ±5 timepoints) for re-use. Last, we fixed a number of bugs, streamlined the code's output to stdout, and made updates necessary for compiling and running on contemporary CUDA hardware and software. Overall, a complete TGMM v2.5 run is typically 30% faster than TGMM 2.0, and produces more accurate results. Regrettably, division classification is still suboptimal even with the above improvements and iterative training of the classifier. Notably, we could not run the convolutional neural network (CNN) division detector included with TGMM 2.0[29] outside of its Docker container, and even there it produced extremely poor results with our datasets. Much work remains in the arena of automated division detection, including not just the identification of division events, but in linking the correct daughter pair to each mother.

Tracking at single cell resolution (Fig. 1D)—Fused .klb image volumes of *Mesp1* lineage, from either the front or side view of each embryo, were used as input for tracking. The empirically-determined optimal F-TGMM configuration parameters used on our datasets are provided in the below table. ProcessStack was run individually (scripted for batch processing) for watershed segmentation of each timepoint's fused volume, followed by a single TGMM call on the entire dataset. Rare, sporadic, dropout of cell linkages were corrected on the resulting TGMM .xml data using a perl script "XMLfinalResult_fix_cell_NaNs.pl," which is included with F-TGMM.

Parameter	TGMM 2.0	F-TGMM v2.5
backgroundThreshold	5	5
radiusMedianFilter	2	2
sigmaGaussianBlurBackground	N/A	20
useBlurredImageForBackgroundDetection	N/A	0.7
weightBlurredImageSubtract	N/A	0.6
minTau	0	0
persistanceSegmentationTau	1	1
betaPercentageOfN_k	1.6	2.5
nuPercentageOfN_k	0.5	0.1
alphaPercentage	0.85	0.75
maxIterEM	50	50
tolLikelihood	1e-6	1e-6
regularizePrecisionMatrixConstants_lambdaMin	0.05	0.02
regularizePrecisionMatrixConstants_lambdaMax	0.8	0.8
regularizePrecisionMatrixConstants_maxExcentricity	16.0	16.0
temporalWindowForLogicalRules	5	5
SLD_lengthTMthr	5	5

Parameter	TGMM 2.0	F-TGMM v2.5
conn3D	74	74
minNucleiSize	1600	1200
maxNucleiSize	20000	10000
maxPercentileTrimSV	0.55	0.8
conn3DsvTrim	6	6
maxNumKNNsupervoxel	10	10
maxDistKNNsupervoxel	40	40
thrSplitScore	−1	−1
thrCellDivisionPlaneDistance	14	14
cellDivisionClassifierMethod	AmatF2013	DominguezM2021
thrCellDivisionWithTemporalWindow	0.45	0.45

Mining and analysis of tracking data (Fig. 1E)—F-TGMM writes .xml tracking solutions, representing the linkages that connect each cell to its past and future self across time. These tracks can be imported directly into MaMuT,[30] a Fiji plugin for annotation and visualization of big datasets. Our fork of the MaMuT plugin (see key resources table) contains improvements to the TGMM import code, enables track vector viewing in 2d (using triangles to indicate spot trajectories in MaMuT viewer – when "display spots" and "display tracks" are enabled, and track display mode is "local in time"), and makes a number of improvements in MaMuT's 3d viewer (recently removed in the upstream mainline repository, but available with our fork) for better performance with large datasets. Moreover, we have written a large collection of scripts (predominantly in Perl, which is pre-installed on Linux and MacOS) for filtering, labeling, subsetting, motion subtracting, merging, analyzing, and exporting from MaMuT datasets (MaMuT Script Library, see key resources table), the features of which are not available in the mainline plugin. These scripts were employed in various operational workflows, for generating the many viewable and analyzable MaMuT datasets presented in this work. Lastly, we updated the SVF package[29] with bug fixes and for use with Python3. Where indicated, we processed TGMM data with SVF to generate long-running vector fields of the dataset for morphometric assessment, which facilitated an overall understanding of tissue deformation during heart development. When individual tracks at single-cell resolution were desired (SVF not indicated), we typically filtered datasets for tracks of 2–4 hour minimum length (i.e. by calling "MaMuT_dataset_split_track_filter.pl"), and occasionally would manually remove tracks not belonging to the cell type of interest (using MaMuT viewer). Starting with a MaMuT .xml dataset (derived either directly from TGMM or via SVF), included scripts facilitate export of spacetime coordinates for each track ("MaMuT_dataset_print_track_coordinates_in_time.pl"), which were summarized for statistical analysis ("MaMuT_track_coordinates_single_data_export.pl") in spreadsheet software or R (see raw data/code repository on Github).

Single cell RNAseq analysis—Single cell wild-type datasets[39,59] were downloaded from public repositories, and analyzed in Seurat[64] v4.0. We tailored the dataset normalization and integration method (CCA, SCtransform) to specific batch effects and

coalescence of like clusters in UMAP space. Initial QC cleanup involved removal of low quality cells, and those belonging to either endoderm or ectoderm lineages. Subsequent clusters were subsetted to depict only pre-cardiac mesoderm and its derivatives. All differential gene expression analysis was performed with FindMarkers in Seurat, and lists of differentially-expressed and non-differentially-expressed genes were inputted into topGO[67] for gene ontology analysis. Pearson correlation was performed on normalized RNA count data. Result visualization was scripted with ggplot2,[68] Seurat,[64] and/or GOplot.[69] Qualitative co-expression feature plots were generated by overlay and assignment of individual feature plots to different channels in Fiji. *Isl1* KO datasets[42,43] were mined for expression of transcripts curated as cluster-identifying markers along a putative vector of SHF differentiation in wild-type single cell analysis.[39] A single cell *Mesp1* KO dataset was generated for a companion manuscript[49], and was analyzed for differential expression of select features relevant to directional migration of mesoderm[50] and related signaling.

Quantification and Statistical Analysis

Mesp1 lineage reporter onset (Fig. S2A–A')—4d image volumes from gastrulation sequences were manually annotated in MaMuT, by identifying mesoderm cells at the x,y,z,t coordinates where they become isolated and sufficiently bright for segmentation / tracking. Each cell was then retrospectively traced to 4d coordinates where it was no longer or just barely visible, usually in more posterior and medial positions abutting the primitive streak region of the embryo. Using the track start/end coordinates, together with coordinates of the anterior midline and primitive streak, derived features such as average velocity and estimated time since departure from primitive streak could be estimated. Mean comparisons were based on Welch t-test. Additional details can be found in the raw data/code for Figure 2 ("Mesp1 reporter and PS analysis.R").

Mesoderm accumulation (Figs. 2B–B', 2C–C', S2G–G')—Using direct TGMM imported data and the MaMuT script library (using 2 iterative calls to "MaMuT_dataset_split_XYZ_coordinate_backward_in_time.pl"), we parsed each embryo (E6.5 – E7.0) into 9 bins comprised of a 3×3 rectangle box pattern as seen in the lateral view, and filtered for QC as described above. For quantification smoothing, each box shares an overlap of 50% of the nearest tracks in each adjacent neighboring box(es). Track birthdate is the timepoint of first appearance of the track. Track density, for each cell within a bin, is the number of other cells present within a radius spanning 12 times the radius of that cell. Track motility was computed as the average of all moving window velocities for a discrete time span (i.e. 30 minutes), incremented each frame over the life of that track. SVF analysis was performed for tissues (i.e. embryonic mesoderm and extraembryonic mesoderm) assigned and painted within SVF's tissue-bw script. Track mean velocity is the total distance traveled divided by the total time span of the track, and is of particular use with SVF analyses. Mean comparisons were based on Welch t-test. Additional details can be found in the raw data/code for Figure 2 ("E6.5 3×3 analysis.R" for Fig. 2B–B', "E6.75 3×3 analysis.R" for Fig. S2G–G', and "E6.5 SVF ExEMvsEM.R" for Fig. 2C–C').

Assessments of cell neighbor relationships and mixing (Figs. 2F–I, S2I–J')—For quantification of separation after cell division, an empty MaMuT dataset

was manually annotated with division nodes and daughter tracks derived from a random assortment of such events in each fused BigDataViewer dataset. Using "MaMuT_track_coordinates_daughter_separation_analyze.pl" from MaMuT script library, mother and daughter positions were exported into a table. Raw measurements were also indexed to a singular length of an average embryo from this stage. For quantification of track position exchanges, we separated each embryo into two bins by cell proximal-distal position, then again by lateral half, resulting in four bins for analysis. We used "MaMuT_track_coordinates_pairwise_analyze.pl" (from MaMuT script library) to analyze tracks in pairwise fashion within the MaMuT datasets, bounded by time and cell distance cutoffs as specified by user (here, co-existent tracks were admitted until t+4.5h into the dataset, and rejected if they were separated by more than 250μm distance in the axis of analysis). Each pair is assessed for its distance offset in the dimension of interest, and those distances can be compared over time to determine whether the tracks exchange position in that dimension. End offsets were first plotted as a function of begin offset, and the relationship was assessed by Pearson correlation coefficient R^2. Next, the offsets were followed in time to determine the number of position exchanges along the axis, and the average number was plotted for each bin and axis. All mean comparisons as described above were made by Welch t-test. Additional details can be found in the raw data/code for Figure 2 ("Mother-daughter separation.R" and "Track crossing.R").

Birth of Smarcd3-F6 progenitors (Fig. 3D–G)—In order to bin tracking results by *Smarcd3*-F6 status, F-TGMM tracking solutions for *Mesp1* lineage progenitors at E7.0 were processed with SVF, using the *Smarcd3*-F6-nGFP channel as a mask for "tissue-bw.py." When "tissue-bw.py" was performed for early (forward propagation) and late (backwards propagation) timepoints, different sets of tracks were included in the F6[+] pool, though late tracks almost always included early tracks as a subset. Using MaMuT script library ("MaMuT_dataset_split_manual_color_quickndirty.pl"), we subtracted the early tracks from the late tracks, and colored all tracks by F6 status: off, on early, or on late (which included the vast majority of on early tracks). Complete painted solutions were visualized with MaMuT. They also underwent uniform sparsification ("MaMuT_dataset_downsample_density_backward_in_time.pl" in MaMuT script library) and were plotted as orthographic projections to depict characteristic migration patterns.

Cell fates of the Smarcd3-F6 lineage (Fig. 3H–H")—Lineage analysis was carried out in fixed embryos imaged by LSFM as described above. Using fused image volumes, we attempted to count all cells in all embryos, assigning them to myocardial or non-myocardial structures. Comparison of their mean contributions to various structures was made by Welch t-test. Additional details can be found in the raw data/code for Figure 3 ("E5-E7 F6 lineage tracing.R" and "F6 lineage tracing quants.ods").

Counting *Mesp1* lineage and Smarcd3-F6 progenitors (Fig. S4C)—Counts of *Mesp1* lineage progenitors were made using live LSFM datasets that had been tracked with F-TGMM, using the number of tracked cells at corresponding timepoints as the initial estimate. Those estimates were further refined by subtracting estimated incidentally-labeled cells (i.e. endoderm, etc). *Smarcd*-F6-nGFP counts were made by performing background

subtraction in Fiji with kernel size 50, then by examining corresponding timepoints with Trackmate's DoG detector with radius 15 and threshold 5. Density of the DoG detection solution was determined by counting number of cells within an arbitrary radius of each cell (i.e. 20μm). Additional details can be found in the raw data/code for Figure 4 ("Cell counts.R").

Cell morphometry during cardiac crescent MET (Fig. 4C)—The volume of *Smarcd3*-F6 progenitors was estimated using a custom Fiji macro ("imagej_macro_klb_folder_estimate_cell_size_using_nGFP-Ai14.txt" in raw data/code for Figure 4), which evaluated *Smarcd3*-F6-nGFP and whole-cell tdTomato (*Mesp1* lineage) at a number of timepoints. In brief, the macro performs dilate alterations and background thresholding on the nGFP channel to create maximal volume regions for the cells of interest (cardiac progenitors), which is intersected with the tdTomato channel containing all *Mesp1* lineage cells. The intersection is measured for integrated intensity, which is divided by the estimated number of cells to yield estimated cell volume. Thickness of the overall crescent was estimated with manual measurements taken in sagittal plane slices. Cell density is summated for each cell as the number of cell neighbors within a stated radius, which is then averaged at individual time lapse frames near stated timepoints. Additional details can be found in the raw data/code for Figure 4 ("Cell density, size, and CC thickness.R").

Quantification of cell adhesion immunostaining on cryosections (Figs. 4D–G and S4H–J)—Maximal Z-projections from 3d images acquired with identical settings were used to assess staining intensity and co-localization for a variety of adhesion-related proteins (pan-CADHERIN, N-CADHERIN, α-CATENIN, γ-CATENIN, MEF2C). Minor but identical linear brightness/contrast adjustments were made to all images for viewing and quantifying. ROIs representing neuroectoderm, cardiac (i.e. MEF2C^{+}) mesoderm, and foregut endoderm were drawn, with three non-mutually-exclusive replicates per image/embryo, and a minimum of three embryos evaluated per condition. ROIs were automatically quantified using a custom macro script in Fiji ("imagej_macro_draw_ROIs_rename_and_quantify_intensity_and_coloc.txt" in raw/data code for Figure 4) that utilized "Measure" and "Colocalization Threshold" methods to obtain intensity and Pearson coefficient (for co-localization assay) in each ROI. Median intensity and Rtotal were assessed across embryos by stage, with mean of each compared by Welch t-test. Additional details can be found in the raw data/code for Figure 4 ("MET cryosection quantifications.R").

Quantifying movement behavior of the heart fields (Figs. 5A–A', 5C–E, S5B, 6C–C')—After cardiac crescent MET, tissues and their descendant structures are revealed morphologically, allowing for F-TGMM tracking solutions to be subsetted into those constituent tissues via SVF. The tracks were analyzed in reverse (i.e. via backward propagation), allowing for an assessment of sites of origin of the three layers principal layers derived during MET (pericardial, myocardial, and endocardial, Fig. 5A–A'). FHF/SHF and JCF were analyzed for net track displacement, which could be assayed with (using "MaMuT_dataset_dataset_subtract_background_and_print_track_coordinates_in_time.pl") or without (using "MaMuT_dataset_print_track_coordinates_in_time.pl") the application of

correction for (i.e. subtraction of nearby) endoderm movement using MaMuT script library (Figs. 5C–C', and 6C–C'). Endoderm correction was especially helpful during foregut folding and involution. For JCF position and motility assessments, we manually quantified F6^{+} cells in maximal z projections, because SVF agglomerates movements into vector fields, destroying nonuniform motility (Figs. 5D–E, S5B). Nuclei orientations were compared using Watson U_2 test, whereas all other measurements were compared as means by Welch t-test. Additional details can be found in the raw data/code for Figure 5 ("3-layer Start Position.R" for Fig. 5A–A', "FHF-SHF movement.R" for Fig. 5C–C', and "JCF motility.R" plus "JCF position and orientation.R" for Figs. 5D–E and S5B) and Figure 6 ("JCF-FHF-SHF movement.R" for Fig. 6C–C').

Comparing *Isl1* mutants with controls (Fig. S7C-E)—3–4 embryos each for *Isl1* KO and control conditions, at 4–7 somite stage, were selected for comparable gross morphology/ appearance, and subjected to fixed LSFM imaging. The MEF2C channel was imported into TrackMate and underwent DoG segmentation with radius 9px and threshold adjusted to yield comparable background detections across all embryos (MEF2C was imaged in two different channels depending on other antibodies used). For total MEF2C counts, TrackMate/MaMuT datasets were split at approximately embryo midline, and half-embryo cell counts were averaged. FHF and SHF membership and phospho-histone H3 labeling of MEF2C cells was quantified using periodic axial slices from each image volume, with FHF-SHF cutoff regions manually assessed by anatomical / morphological appearance using time-lapse LSFM footage from *Mef2c*AHF lineage tracing experiments (Figs. 5B–B', S5A–A") as a reference. Means were compared with Welch t-test. Additional details can be found in the raw data/code for Figure S7 ("Early somite Isl1 KO quantifications.R").

Comparing *Mesp1* mutants with controls (Fig. 7C–C")—Since we had already determined that mesoderm accumulation occurs by diagonal spatiotemporal gradient, we compared cells from mutant and control embryos by assigning them to a position along that axis (rather than by membership to 3×3 spatial grids). We applied similar metrics utilized previously. Motility was computed as the average displacement sampled over 30-minute moving windows, and cell density as the average number of other cells counted within a 12-nuclei-radius from each cell. Additionally, track trajectories were scored in the lateral view, using the start and end coordinates to determine the directionality (in the orthographic lateral view). Trajectory angles (anterior at 0°, proximal at 90°) were calculated for each track in the orthographic lateral view, using a 2d vector from its start coordinate to end coordinate. Density distributions of all trajectory angles were plotted in polar space, and were compared with Watson U_2 tests. All other measurements were compared as means by Welch t-test. Additional details can be found in the raw data/code for Figure 7 ("Gradient MaMuT.R").

Supplementary Material

Refer to Web version on PubMed Central for supplementary material.

Acknowledgements

Inclusion and diversity

We support inclusive, diverse, and equitable conduct of research. One or more of the authors of this paper self-identifies as an underrepresented ethnic minority in their field of research or within their geographical location.

References

1. de la Cruz MV, Castillo MM, Villavicencio L, Valencia A, and Moreno-Rodriguez RA (1997). Primitive interventricular septum, its primordium, and its contribution in the definitive interventricular septum: in vivo labelling study in the chick embryo heart. Anat. Rec 247, 512–520. 10.1002/(SICI)1097-0185(199704)247:4<512::AID-AR10>3.0.CO;2-S. [PubMed: 9096791]

2. Cui C, Cheuvront TJ, Lansford RD, Moreno-Rodriguez RA, Schultheiss TM, and Rongish BJ (2009). Dynamic positional fate map of the primary heart-forming region. Dev. Biol 332, 212–222. 10.1016/j.ydbio.2009.05.570. [PubMed: 19497319]

3. Evans SM, Yelon D, Conlon FL, and Kirby ML (2010). Myocardial Lineage Development. Circ. Res 107, 1428–1444. 10.1161/CIRCRESAHA.110.227405. [PubMed: 21148449]

4. Kelly RG, Buckingham ME, and Moorman AF (2014). Heart fields and cardiac morphogenesis. Cold Spring Harb. Perspect. Med 4. 10.1101/cshperspect.a015750.

5. Meilhac SM, Esner M, Kelly RG, Nicolas J-F, and Buckingham ME (2004). The clonal origin of myocardial cells in different regions of the embryonic mouse heart. Dev. Cell 6, 685–698. [PubMed: 15130493]

6. Devine WP, Wythe JD, George M, Koshiba-Takeuchi K, and Bruneau BG (2014). Early patterning and specification of cardiac progenitors in gastrulating mesoderm. eLife 3. 10.7554/eLife.03848.

7. Lescroart F, Chabab S, Lin X, Rulands S, Paulissen C, Rodolosse A, Auer H, Achouri Y, Dubois C, Bondue A, et al. (2014). Early lineage restriction in temporally distinct populations of Mesp1 progenitors during mammalian heart development. Nat. Cell Biol 16, 829–840. 10.1038/ncb3024. [PubMed: 25150979]

8. Saga Y, Miyagawa-Tomita S, Takagi A, Kitajima S, Miyazaki J. i, and Inoue T (1999). MesP1 is expressed in the heart precursor cells and required for the formation of a single heart tube. Development. 126, 3437–3447. [PubMed: 10393122]

9. Tyser RCV, Ibarra-Soria X, McDole K, Arcot Jayaram S, Godwin J, van den Brand TAH, Miranda AMA, Scialdone A, Keller PJ, Marioni JC, et al. (2021). Characterization of a common progenitor pool of the epicardium and myocardium. Science 371, eabb2986. 10.1126/science.abb2986. [PubMed: 33414188]

10. Zhang Q, Carlin D, Zhu F, Cattaneo P, Ideker T, Evans SM, Bloomekatz J, and Chi NC (2021). Unveiling Complexity and Multipotentiality of Early Heart Fields. Circ. Res 129, 474–487. 10.1161/CIRCRESAHA.121.318943. [PubMed: 34162224]

11. Später D, Abramczuk MK, Buac K, Zangi L, Stachel MW, Clarke J, Sahara M, Ludwig A, and Chien KR (2013). A HCN4+ cardiomyogenic progenitor derived from the first heart field and human pluripotent stem cells. Nat. Cell Biol 15, 1098–1106. 10.1038/ncb2824. [PubMed: 23974038]

12. Cai C-L, Liang X, Shi Y, Chu P-H, Pfaff SL, Chen J, and Evans S (2003). Isl1 Identifies a Cardiac Progenitor Population that Proliferates Prior to Differentiation and Contributes a Majority of Cells to the Heart. Dev. Cell 5, 877–889. [PubMed: 14667410]

13. Kelly RG, Brown NA, and Buckingham ME (2001). The arterial pole of the mouse heart forms from Fgf10-expressing cells in pharyngeal mesoderm. Dev. Cell 1, 435–440. [PubMed: 11702954]

14. Ivanovitch K, Soro-Barrio P, Chakravarty P, Jones RA, Bell DM, Mousavy Gharavy SN, Stamataki D, Delile J, Smith JC, and Briscoe J (2021). Ventricular, atrial, and outflow tract heart progenitors arise from spatially and molecularly distinct regions of the primitive streak. PLoS Biol. 19, e3001200. 10.1371/journal.pbio.3001200. [PubMed: 33999917]

15. Abu-Issa R, and Kirby ML (2008). Patterning of the heart field in the chick. Dev. Biol 319, 223–233. 10.1016/j.ydbio.2008.04.014. [PubMed: 18513714]

16. Aleksandrova A, Czirok A, Kosa E, Galkin O, Cheuvront TJ, and Rongish BJ (2015). The endoderm and myocardium join forces to drive early heart tube assembly. Dev. Biol 404, 40–54. 10.1016/j.ydbio.2015.04.016. [PubMed: 25952622]

17. Kidokoro H, Yonei-Tamura S, Tamura K, Schoenwolf GC, and Saijoh Y (2018). The heart tube forms and elongates through dynamic cell rearrangement coordinated with foregut extension. Development. 145. 10.1242/dev.152488.

18. Aguilera-Castrejon A, Oldak B, Shani T, Ghanem N, Itzkovich C, Slomovich S, Tarazi S, Bayerl J, Chugaeva V, Ayyash M, et al. (2021). Ex utero mouse embryogenesis from pre-gastrulation to late organogenesis. Nature 593, 119–124. 10.1038/s41586-021-03416-3. [PubMed: 33731940]

19. Glanville-Jones HC, Woo N, and Arkell RM (2013). Successful whole embryo culture with commercially available reagents. Int. J. Dev. Biol 57, 61–67. 10.1387/ijdb.120098ra. [PubMed: 23585354]

20. Harrison SE, Sozen B, Christodoulou N, Kyprianou C, and Zernicka-Goetz M (2017). Assembly of embryonic and extraembryonic stem cells to mimic embryogenesis in vitro. Science 356. 10.1126/science.aal1810.

21. Tam PP (1998). Postimplantation mouse development: whole embryo culture and micro-manipulation. Int. J. Dev. Biol 42, 895–902. [PubMed: 9853819]

22. Saykali B, Mathiah N, Nahaboo W, Racu M-L, Hammou L, Defrance M, and Migeotte I (2019). Distinct mesoderm migration phenotypes in extra-embryonic and embryonic regions of the early mouse embryo. eLife 8, e42434. 10.7554/eLife.42434. [PubMed: 30950395]

23. Ivanovitch K, Temiño S, and Torres M (2017). Live imaging of heart tube development in mouse reveals alternating phases of cardiac differentiation and morphogenesis. eLife 6. 10.7554/eLife.30668.

24. Falk HJ, Tomita T, Mönke G, McDole K, and Aulehla A (2022). Imaging the onset of oscillatory signaling dynamics during mouse embryo gastrulation. Development. 149, dev200083. 10.1242/dev.200083. [PubMed: 35686648]

25. Ichikawa T, Nakazato K, Keller PJ, Kajiura-Kobayashi H, Stelzer EHK, Mochizuki A, and Nonaka S (2013). Live imaging of whole mouse embryos during gastrulation: migration analyses of epiblast and mesodermal cells. PloS One 8, e64506. 10.1371/journal.pone.0064506. [PubMed: 23861733]

26. Udan RS, Piazza VG, Hsu C-W, Hadjantonakis A-K, and Dickinson ME (2014). Quantitative imaging of cell dynamics in mouse embryos using light-sheet microscopy. Development. 141, 4406–4414. 10.1242/dev.111021. [PubMed: 25344073]

27. Yue Y, Zong W, Li X, Li J, Zhang Y, Wu R, Liu Y, Cui J, Wang Q, Bian Y, et al. (2020). Long-term, in toto live imaging of cardiomyocyte behaviour during mouse ventricle chamber formation at single-cell resolution. Nat. Cell Biol 22, 332–340. 10.1038/s41556-020-0475-2. [PubMed: 32123336]

28. Hörl D, Rojas Rusak F, Preusser F, Tillberg P, Randel N, Chhetri RK, Cardona A, Keller PJ, Harz H, Leonhardt H, et al. (2019). BigStitcher: reconstructing high-resolution image datasets of cleared and expanded samples. Nat. Methods 16, 870–874. 10.1038/s41592-019-0501-0. [PubMed: 31384047]

29. McDole K, Guignard L, Amat F, Berger A, Malandain G, Royer LA, Turaga SC, Branson K, and Keller PJ (2018). In Toto Imaging and Reconstruction of Post-Implantation Mouse Development at the Single-Cell Level. Cell 175, 859–876.e33. 10.1016/j.cell.2018.09.031. [PubMed: 30318151]

30. Wolff C, Tinevez J-Y, Pietzsch T, Stamataki E, Harich B, Guignard L, Preibisch S, Shorte S, Keller PJ, Tomancak P, et al. (2018). Multi-view light-sheet imaging and tracking with the MaMuT software reveals the cell lineage of a direct developing arthropod limb. eLife 7. 10.7554/eLife.34410.

31. Hansen PC, Nagy JG, and O'Leary DP (2006). Deblurring Images: Matrices, Spectra, and Filtering (SIAM).

32. Preibisch S, Amat F, Stamataki E, Sarov M, Singer RH, Myers E, and Tomancak P (2014). Efficient Bayesian-based multiview deconvolution. Nat. Methods 11, 645–648. 10.1038/nmeth.2929. [PubMed: 24747812]

33. Wendykier P, and Nagy JG (2008). Large-Scale Image Deblurring in Java. In Computational Science – ICCS 2008 Lecture Notes in Computer Science., Bubak M, Albada G. D. van, Dongarra J, and Sloot PMA, eds. (Springer), pp. 721–730. 10.1007/978-3-540-69384-0_77.

34. Schindelin J, Arganda-Carreras I, Frise E, Kaynig V, Longair M, Pietzsch T, Preibisch S, Rueden C, Saalfeld S, Schmid B, et al. (2012). Fiji: an open-source platform for biological-image analysis. Nat. Methods 9, 676–682. 10.1038/nmeth.2019. [PubMed: 22743772]

35. Probst S, Sagar, Tosic J Schwan C, Grün D, and Arnold SJ (2021). Spatiotemporal sequence of mesoderm and endoderm lineage segregation during mouse gastrulation. Development 148, dev193789. 10.1242/dev.193789. [PubMed: 33199445]

36. Lescroart F, Wang X, Lin X, Swedlund B, Gargouri S, Sànchez-Dànes A, Moignard V, Dubois C, Paulissen C, Kinston S, et al. (2018). Defining the earliest step of cardiovascular lineage segregation by single-cell RNA-seq. Science 359, 1177–1181. 10.1126/science.aao4174. [PubMed: 29371425]

37. Pei D, Shu X, Gassama-Diagne A, and Thiery JP (2019). Mesenchymal-epithelial transition in development and reprogramming. Nat. Cell Biol 21, 44–53. 10.1038/s41556-018-0195-z. [PubMed: 30602762]

38. Schlueter J, and Mikawa T (2018). Body Cavity Development Is Guided by Morphogen Transfer between Germ Layers. Cell Rep. 24, 1456–1463. 10.1016/j.celrep.2018.07.015. [PubMed: 30089257]

39. de Soysa TY, Ranade SS, Okawa S, Ravichandran S, Huang Y, Salunga HT, Schricker A, Del Sol A, Gifford CA, and Srivastava D (2019). Single-cell analysis of cardiogenesis reveals basis for organ-level developmental defects. Nature 572, 120–124. 10.1038/s41586-019-1414-x. [PubMed: 31341279]

40. Cortes C, Francou A, De Bono C, and Kelly RG (2018). Epithelial Properties of the Second Heart Field. Circ. Res 122, 142–154. 10.1161/CIRCRESAHA.117.310838. [PubMed: 29301846]

41. Jia G, Preussner J, Chen X, Guenther S, Yuan X, Yekelchyk M, Kuenne C, Looso M, Zhou Y, Teichmann S, et al. (2018). Single cell RNA-seq and ATAC-seq analysis of cardiac progenitor cell transition states and lineage settlement. Nat. Commun 9, 4877. 10.1038/s41467-018-07307-6. [PubMed: 30451828]

42. Quaranta R, Fell J, Rühle F, Rao J, Piccini I, Araúzo-Bravo MJ, Verkerk AO, Stoll M, and Greber B (2018). Revised roles of ISL1 in a hES cell-based model of human heart chamber specification. eLife 7. 10.7554/eLife.31706.

43. Gao R, Liang X, Cheedipudi S, Cordero J, Jiang X, Zhang Q, Caputo L, Günther S, Kuenne C, Ren Y, et al. (2019). Pioneering function of Isl1 in the epigenetic control of cardiomyocyte cell fate. Cell Res. 29, 486–501. 10.1038/s41422-019-0168-1. [PubMed: 31024170]

44. Kathiriya IS, Nora EP, and Bruneau BG (2015). Investigating the transcriptional control of cardiovascular development. Circ. Res 116, 700–714. 10.1161/CIRCRESAHA.116.302832. [PubMed: 25677518]

45. Gordon DM, Cunningham D, Zender G, Lawrence PJ, Penaloza JS, Lin H, Fitzgerald-Butt SM, Myers K, Duong T, Corsmeier DJ, et al. (2022). Exome sequencing in multiplex families with left-sided cardiac defects has high yield for disease gene discovery. PLoS Genet. 18, e1010236. 10.1371/journal.pgen.1010236. [PubMed: 35737725]

46. Yang Y, Xia Y, Wu Y, Huang S, Teng Y, Liu X, Li P, Chen J, and Zhuang J (2019). Ankyrin repeat domain 1: A novel gene for cardiac septal defects. J. Gene Med 21, e3070. 10.1002/jgm.3070. [PubMed: 30659708]

47. Ajima R, Sakakibara Y, Sakurai-Yamatani N, Muraoka M, and Saga Y (2021). Formal proof of the requirement of MESP1 and MESP2 in mesoderm specification and their transcriptional control via specific enhancers in mice. Development. 148, dev194613. 10.1242/dev.194613. [PubMed: 34679163]

48. Chiapparo G, Lin X, Lescroart F, Chabab S, Paulissen C, Pitisci L, Bondue A, and Blanpain C (2016). Mesp1 controls the speed, polarity, and directionality of cardiovascular progenitor migration. J. Cell Biol 213, 463–477. 10.1083/jcb.201505082. [PubMed: 27185833]

49. Krup AL, Winchester SAB, Ranade SS, Agrawal A, Devine WP, Sinha T, Choudhary K, Dominguez MH, Thomas R, Black BL, Srivastava D, and Bruneau BG (2022). A Mesp1-dependent developmental breakpoint in transcriptional and epigenomic specification of early cardiac precursors. bioRxiv 2022.08.22.504863. 10.1101/2022.08.22.504863.

50. Keller R (2005). Cell migration during gastrulation. Curr. Opin. Cell Biol 17, 533–541. 10.1016/j.ceb.2005.08.006. [PubMed: 16099638]

51. Bénazéraf B, Francois P, Baker RE, Denans N, Little CD, and Pourquié O (2010). A random cell motility gradient downstream of FGF controls elongation of an amniote embryo. Nature 466, 248–252. 10.1038/nature09151. [PubMed: 20613841]

52. Regev I, Guevorkian K, Gupta A, Pourquié O, and Mahadevan L (2022). Rectified random cell motility as a mechanism for embryo elongation. Development. 149, dev199423. 10.1242/dev.199423. [PubMed: 35344041]

53. Fulton T, Trivedi V, Attardi A, Anlas K, Dingare C, Arias AM, and Steventon B (2020). Axis Specification in Zebrafish Is Robust to Cell Mixing and Reveals a Regulation of Pattern Formation by Morphogenesis. Curr. Biol. CB 30, 2984–2994.e3. 10.1016/j.cub.2020.05.048. [PubMed: 32559447]

54. Ferretti E, and Hadjantonakis A-K (2019). Mesoderm specification and diversification: from single cells to emergent tissues. Curr. Opin. Cell Biol 61, 110–116. 10.1016/j.ceb.2019.07.012. [PubMed: 31476530]

55. Shahbazi MN, and Zernicka-Goetz M (2018). Deconstructing and reconstructing the mouse and human early embryo. Nat. Cell Biol 20, 878–887. 10.1038/s41556-018-0144-x. [PubMed: 30038253]

56. Donà E, Barry JD, Valentin G, Quirin C, Khmelinskii A, Kunze A, Durdu S, Newton LR, Fernandez-Minan A, Huber W, et al. (2013). Directional tissue migration through a self-generated chemokine gradient. Nature 503, 285–289. 10.1038/nature12635. [PubMed: 24067609]

57. Dodou E, Verzi MP, Anderson JP, Xu S-M, and Black BL (2004). Mef2c is a direct transcriptional target of ISL1 and GATA factors in the anterior heart field during mouse embryonic development. Development 131, 3931–3942. 10.1242/dev.01256. [PubMed: 15253934]

58. Bedzhov I, and Zernicka-Goetz M (2014). Self-Organizing Properties of Mouse Pluripotent Cells Initiate Morphogenesis upon Implantation. Cell 156, 1032–1044. 10.1016/j.cell.2014.01.023. [PubMed: 24529478]

59. Tyser RC, Miranda AM, Chen C-M, Davidson SM, Srinivas S, and Riley PR (2016). Calcium handling precedes cardiac differentiation to initiate the first heartbeat. eLife 5. 10.7554/eLife.17113.

60. Cho CH, Kim SS, Jeong MJ, Lee CO, and Shin HS (2000). The Na+ -Ca2+ exchanger is essential for embryonic heart development in mice. Mol. Cells 10, 712–722. 10.1007/s10059-000-0712-2. [PubMed: 11211878]

61. Koushik SV, Wang J, Rogers R, Moskophidis D, Lambert NA, Creazzo TL, and Conway SJ (2001). Targeted inactivation of the sodium-calcium exchanger (Ncx1) results in the lack of a heartbeat and abnormal myofibrillar organization. FASEB J. Off. Publ. Fed. Am. Soc. Exp. Biol 15, 1209–1211. 10.1096/fj.00-0696fje.

62. Lowe DG (2004). Distinctive Image Features from Scale-Invariant Keypoints. Int. J. Comput. Vis 60, 91–110. 10.1023/B:VISI.0000029664.99615.94.

63. Perbellini F, Liu AKL, Watson SA, Bardi I, Rothery SM, and Terracciano CM (2017). Free-of-Acrylamide SDS-based Tissue Clearing (FASTClear) for three dimensional visualization of myocardial tissue. Sci. Rep 7, 1–9. 10.1038/s41598-017-05406-w. [PubMed: 28127051]

64. Hao Y, Hao S, Andersen-Nissen E, Mauck WM, Zheng S, Butler A, Lee MJ, Wilk AJ, Darby C, Zager M, et al. (2021). Integrated analysis of multimodal single-cell data. Cell 184, 3573–3587.e29. 10.1016/j.cell.2021.04.048. [PubMed: 34062119]

65. Amat F, Lemon W, Mossing DP, McDole K, Wan Y, Branson K, Myers EW, and Keller PJ (2014). Fast, accurate reconstruction of cell lineages from large-scale fluorescence microscopy data. Nat. Methods 11, 951–958. 10.1038/nmeth.3036. [PubMed: 25042785]

66. Tinevez J-Y, Perry N, Schindelin J, Hoopes GM, Reynolds GD, Laplantine E, Bednarek SY, Shorte SL, and Eliceiri KW (2017). TrackMate: An open and extensible platform for single-particle tracking. Methods San Diego Calif 115, 80–90. 10.1016/j.ymeth.2016.09.016. [PubMed: 27713081]

67. Alexa A, and Rahnenfuhrer J (2022). topGO: Enrichment Analysis for Gene Ontology. 10.18129/B9.bioc.topGO.

68. Wickham H (2016). ggplot2: Elegant Graphics for Data Analysis 2nd ed. 2016 edition. (Springer).

69. Walter W, Sánchez-Cabo F, and Ricote M (2015). GOplot: an R package for visually combining expression data with functional analysis. Bioinforma. Oxf. Engl 31, 2912–2914. 10.1093/bioinformatics/btv300.

Highlights

- improved workflow for in toto reconstruction of mouse embryogenesis, single cell tracking

- patterned filling of cardiac mesoderm without linear paths, but with marked cell mixing

- cardiac fields exhibit surprising collective and individual spatiotemporal behaviors

- *Mesp1* mutant mesoderm progenitors maintain motility but lose directionality
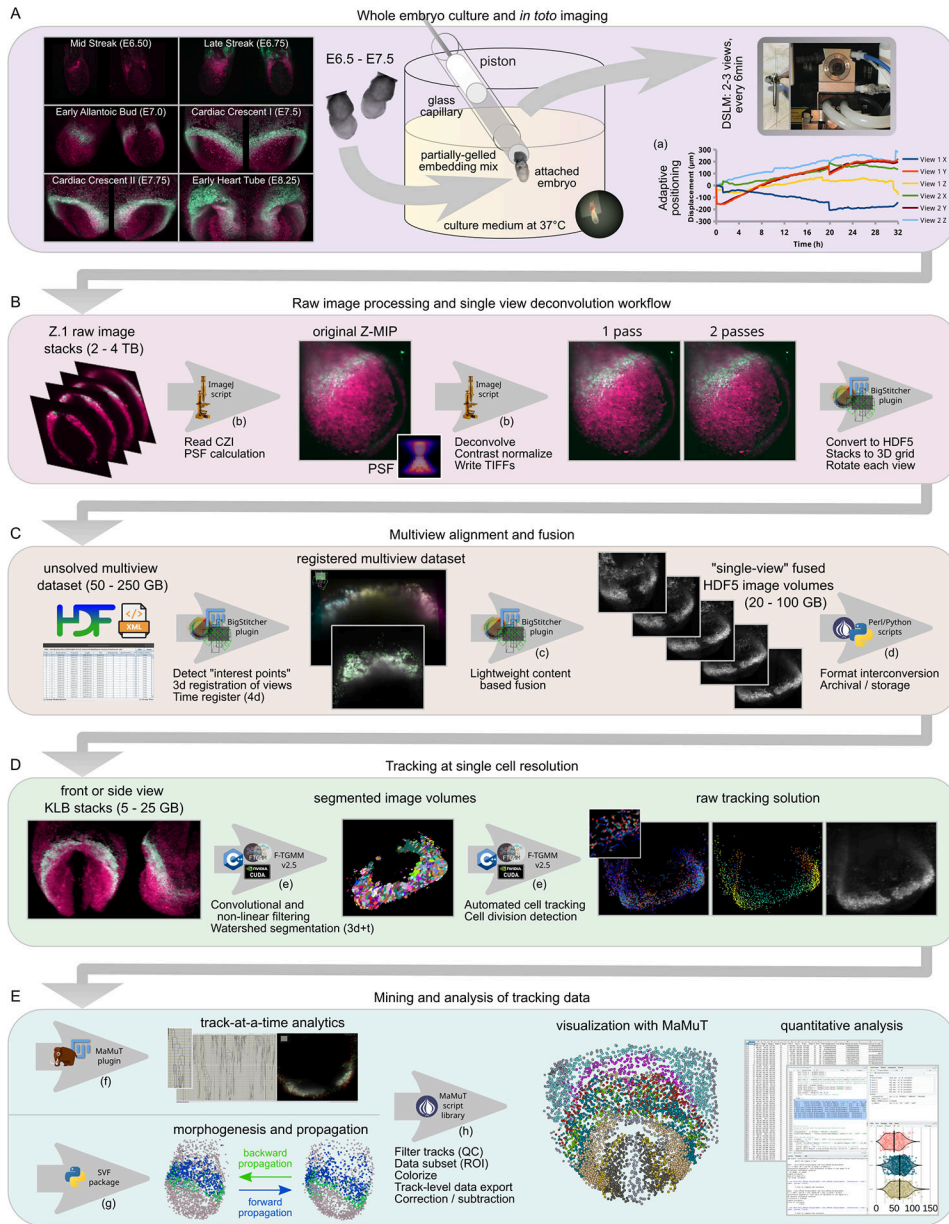
Figure 1: Comprehensive workflow for quantitative analysis of embryogenesis by live LSFM
A. Biology and microscopy protocol. Red signal: *Mesp1* lineage, green signal: *Smarcd3*-F6-nGFP. ZLAPS adaptive positioning example is shown, demonstrating shifts of two views' XYZ positions needed to maintain the embryo in the center of the view. **B**. Initial computational workflow, depicting macro-based batch deconvolution, filtering, and image import to BigStitcher. **C**. Multiview alignment to generate single image volumes for each channel and timepoint. **D**. Improved tracking with F-TGMM v2.5. **E**. F-TGMM results can be refined using SVF to generate long-track morphodynamic models, or can be examined raw. MaMuT script library annotates, filters, subsets, combines, and exports data. Lower case letters correspond with repositories listed in key resources table.
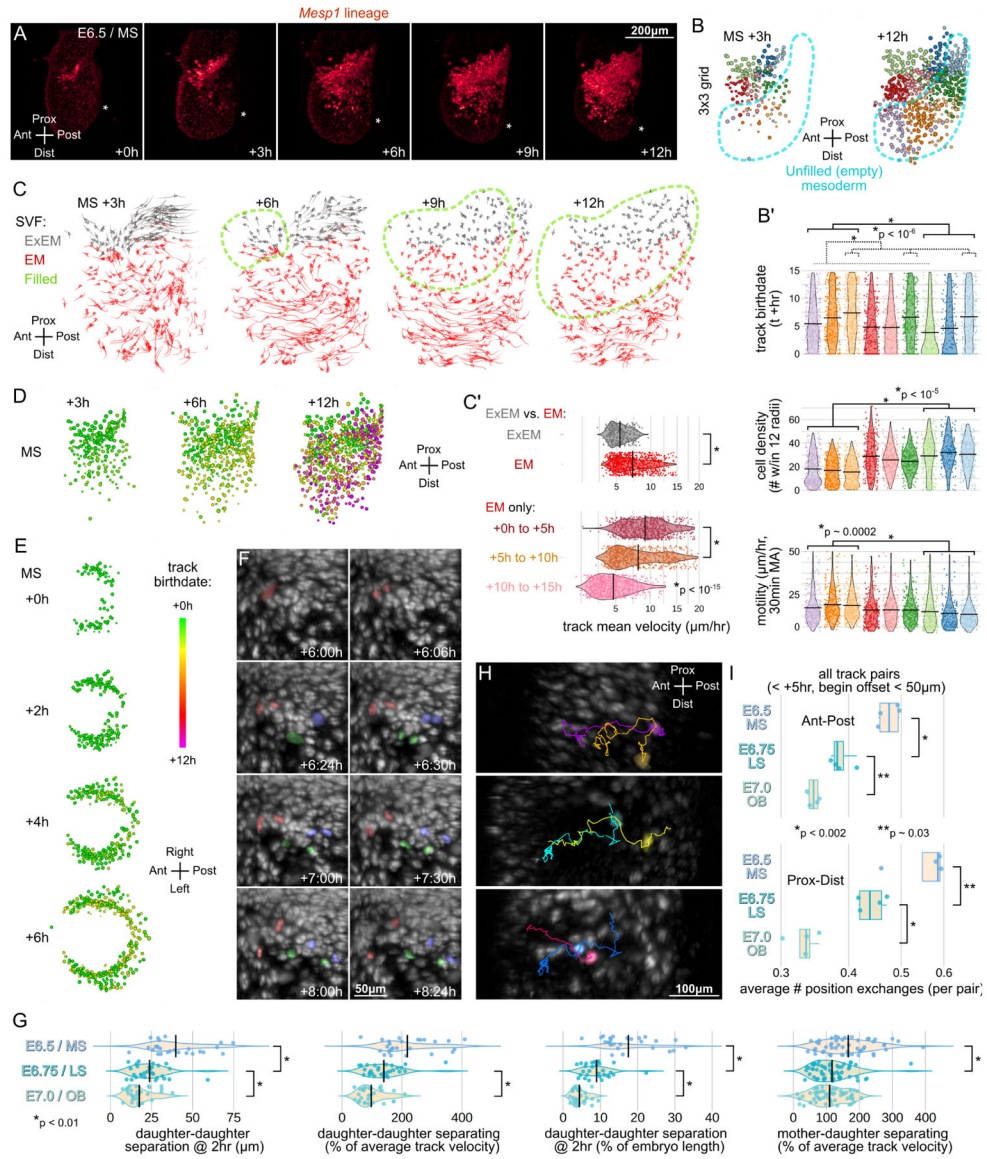
Figure 2: A spatiotemporal gradient of mesoderm accumulation

A. Time-lapse whole-embryo LSFM imaging of *Mesp1* lineage at E6.5/MS, showing lateral view left-half max projections. Asterisks denote anterior extent of primitive streak. **B**. Side views of a TGMM/MaMuT reconstructed E6.5/MS embryo during live imaging, with all tracks retrospectively partitioned onto a 3×3 grid. **B'**. TGMM tracks analyzed from +0h to +15h for birthdate, motility, and cell density. **C**. TGMM/SVF reconstruction of MS anterior mesoderm migration, in orthographic projection with uniform sparsification. Extraembryonic (ExEM) and embryonic (EM) compartments are colored. **C'**. Quantification of this SVF series. **D-E**. TGMM reconstruction E6.5 embryo live imaging, cells painted by track birthdate. **F**. Three manually annotated, randomly dispersed, division events are overlayed in false color (division nodes and daughter cells) on single sided, lateral Z-projections from live imaging experiments at E6.5/MS. **G**. Quantification of division cohorts from E6.5/MS to E7.0/EB demonstrates separation behaviors of daughters following

division (see **F** above). **H-I**. Analysis of TGMM track crossing behavior, using pairwise analysis of tracks from E6.5/MS to E7.0/EB. Three unrelated pairs of nearby tracks during a MS acquisition are shown in **H**. **I**. Track pair crossing events (each point is the mean of a half-embryo subset) are assessed in the anterior-posterior (top panel) and proximal-distal (bottom panel) axes, as a function of embryo stage.
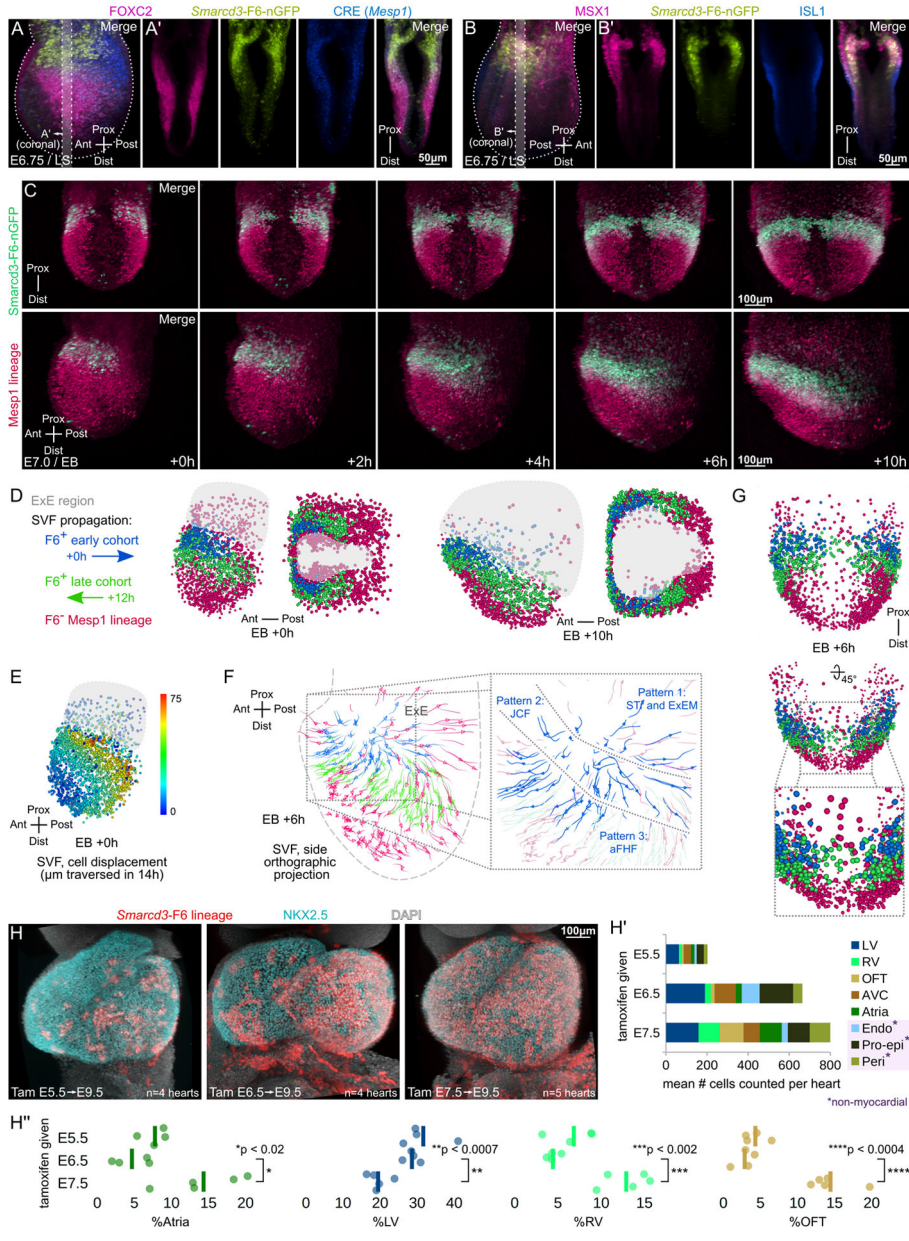
Figure 3: Birth of the Smarcd3-F6 cardiac progenitors

A-B. LSFM imaging of fixed E6.75/LS embryos shows that Mesp1-lineage-derived embryonic mesoderm is divided into two compartments, a distal FOXC2$^+$;F6$^-$ compartment (**A**), and a proximal MSX1$^+$;F6$^+$ compartment (**B**). **A'**,**B'**: Coronal slices from **A,B. C**. Time-lapse whole-embryo imaging at E7.0/EB, demonstrating the onset and expansion of *Smarcd3*-F6-nGFP+ progenitors. Fused image sequence in frontal (top row) and through-view right-half (bottom row) max projections. **D**. TGMM and SVF reconstruction of the total Mesp1-lineage population of cells, painted by F6 status: F6$^-$, or either F6$^+$ at the start (early cohort), or F6$^+$ after twelve hours (late cohort). MaMuT display of the TGMM/SVF solution at the times indicated, from the side view (first and third panels in **D**), and Mercator projection (second and fourth panels in **D**). **E**. The same TGMM/SVF time-lapse sequence

shown in **D** is depicted in MaMuT from the side view, with cells colored by the total displacement of their tracks. **F**. The TGMM/SVF solution is displayed in MaMuT (at the timepoint indicated) using an orthographic projection from the side, to depict the three classes of early F6$^+$ cohort cells (inset). **G**. The midline breach forming the arch of the crescent is made up of both early- and late cohort F6$^+$ progenitors. **H-H**". Lineage tracing using *Smarcd3*-F6-CreERT2;Ai14 mice. NKX2.5 and DAPI counter-labeling as shown.
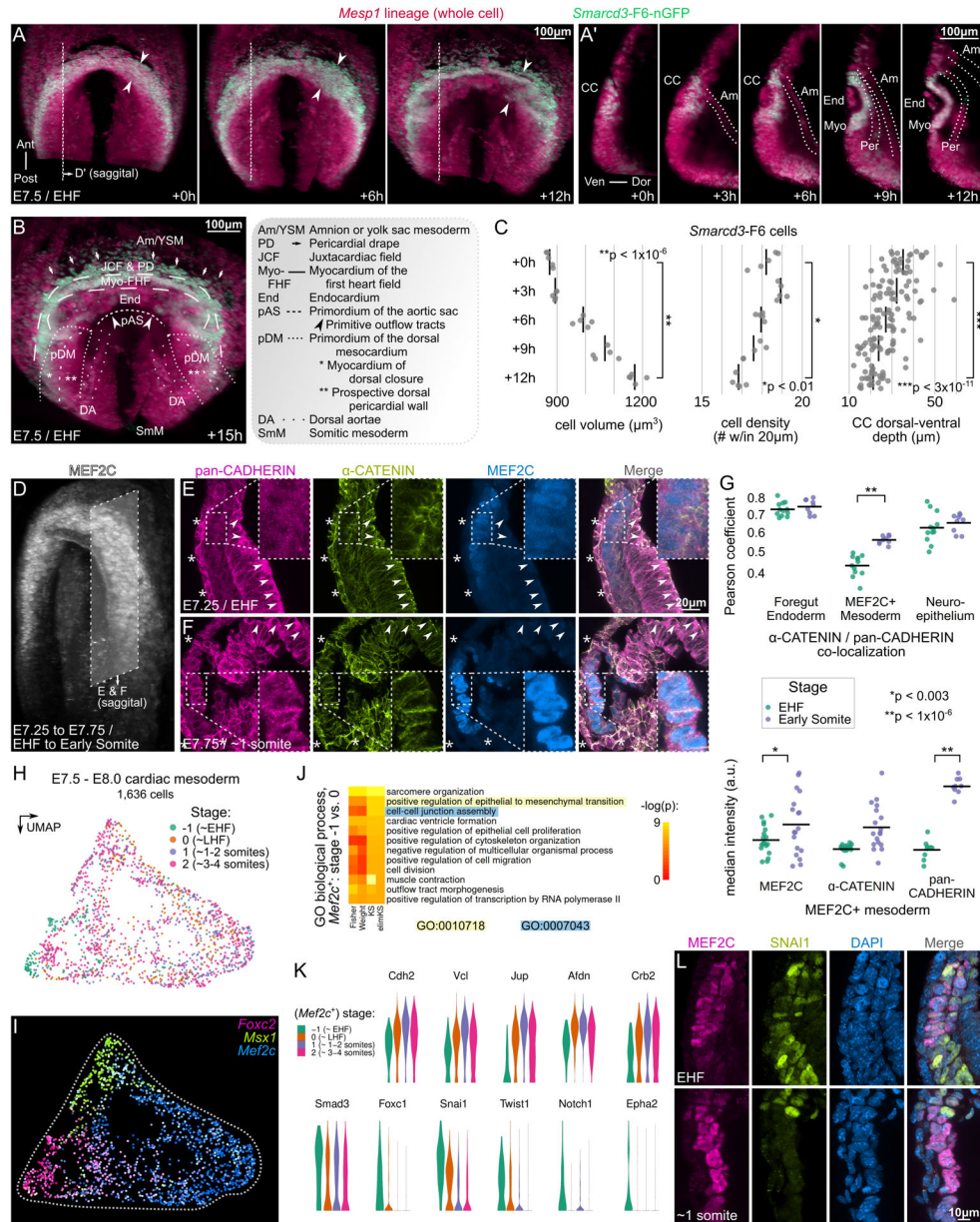
Figure 4: Mesenchymal-epithelial transition of the cardiac crescent

A-B. Time-lapse whole-embryo LSFM imaging at E7.25-E7.5 demonstrates splitting of the mesoderm and mesenchymal-epithelial transition of the cardiac crescent (arrowheads in **A**). Frontal (ventral) maximum projection (**A**) and single cutaway sagittal sections (**A'**). Am = amnion, Myo = myocardium, End = endocardium, Per = pericardium, CC = cardiac crescent. B. Annotation of early cardiac structures at +21h, **C**. Multi-modal estimations of *Smarcd3*-F6 cells during above sequence. **D**. Oblique 3d projection of cardiac crescent in LSFM imaged E7.5 / LHF stage embryo, showing region of sections in subsequent panels. **E-F**. Representative 14μm sagittal cryosections from EHF (**E**) and early somite (**F**) mouse embryos, examined by immunohistochemistry. Asterisks = foregut endoderm; arrowheads = apical neuroepithelium. **G**. Quantifications of pan-CADHERIN and α-CATENIN channel

overlap (i.e. co-localization, upper plots) in indicated regions, as well as single-channel signal intensity for indicated proteins within MEF2C$^+$ cardiac progenitors (lower plots). **H-K**. Analysis of single cell RNA sequencing of early cardiac crescents at fine embryo stage resolution.[9] UMAP representation of earliest four stages of cardiac mesoderm (**H**), with qualitative co-expression of *Foxc2*, *Msx1*, and *Mef2c* (**I**). Differential expression testing of *Mef2c*$^+$ cells between earliest stages −1 and 0 was performed, with most significant 12 GO BP categories in **J**. Violin plots of select gene members of GO:0010718 and GO:0007043 is depicted per stage, subset by *Mef2c*$^+$, in **K. L**. 14μm immunostained sagittal cryosections from EHF (**H**) and early somite (**I**) mouse embryos, focused on MEF2C and SNAI1.
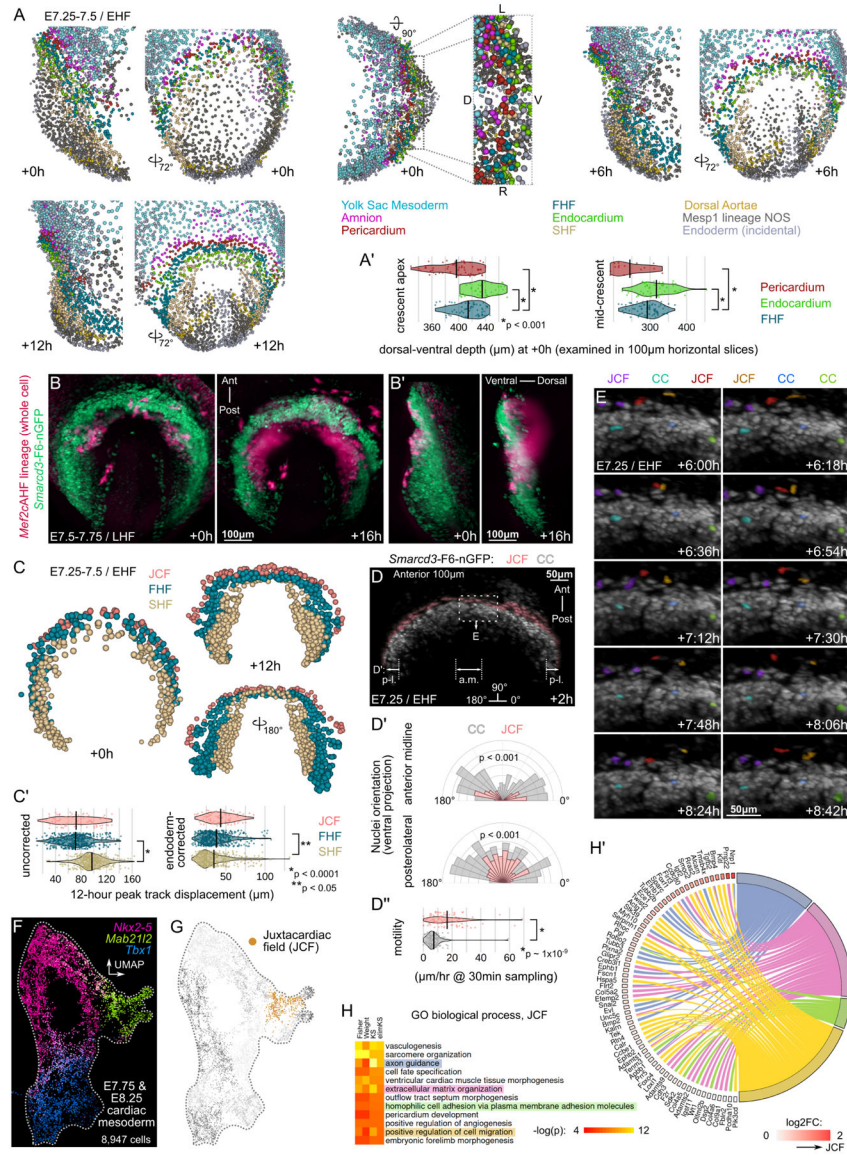
Figure 5: Movement of cell populations during crescent MET

A-A'. SVF reconstructions of cardiac crescent MET at indicated timepoints (**A**). Cell tracks, coordinates, and tissue assignments (color legend shown in **A**) are derived from backwards-propagated SVF data. **A'**. Positions of pericardial, myocardial, and endocardial cells in the dorsal-ventral axis determined through backwards propagation, for cells near the anterior crescent apex (left) or in the middle of the crescent (right). **B-B'**. Time-lapse whole-embryo LSFM at E7.5-E7.75/LHF using the *Mef2c*AHF lineage reporter, with ventral (**B**) and through-view right-half (**B'**) max projections. **C-C'**. SVF reconstruction at indicated timepoints from dorsal and ventral views, showing only FHF, SHF, and JCF. Peak SVF track displacement is quantified (**C'**, without or with endoderm correction). **D**. JCF cells are false colored in pink to highlight their position and orientation. **D'**. Quantification of long-axis orientations of nuclei comparing JCF to cardiac crescent ("CC") cells (**D'**, top panel corresponds to anterior midline 'a.m.' in **D**, lower panel corresponds to posterolateral

crescent 'p-l.' in **D**), with p-values from Watson U_2 test. **D"**. Motility of JCF and CC cells. **E**. Time-lapse sequence from ventral partial max projection images using false colors to highlight a sample of six cells (3 JCF, 3 CC) throughout the sequence. **F-G**. Single cell RNA sequencing analysis of E7.75 and E8.25 cardiac mesoderm,[39] with identification of the JCF cluster (**G**) by qualitative co-expression with *Nkx2–5*, *Tbx1*, and *Mab21l2* (**F**). **H**. Twelve most significant GO BP categories for marker genes defining JCF. **H'**. Five interesting BP terms inspected by gene membership and log2FC differential expression (JCF versus remaining cardiac mesoderm).
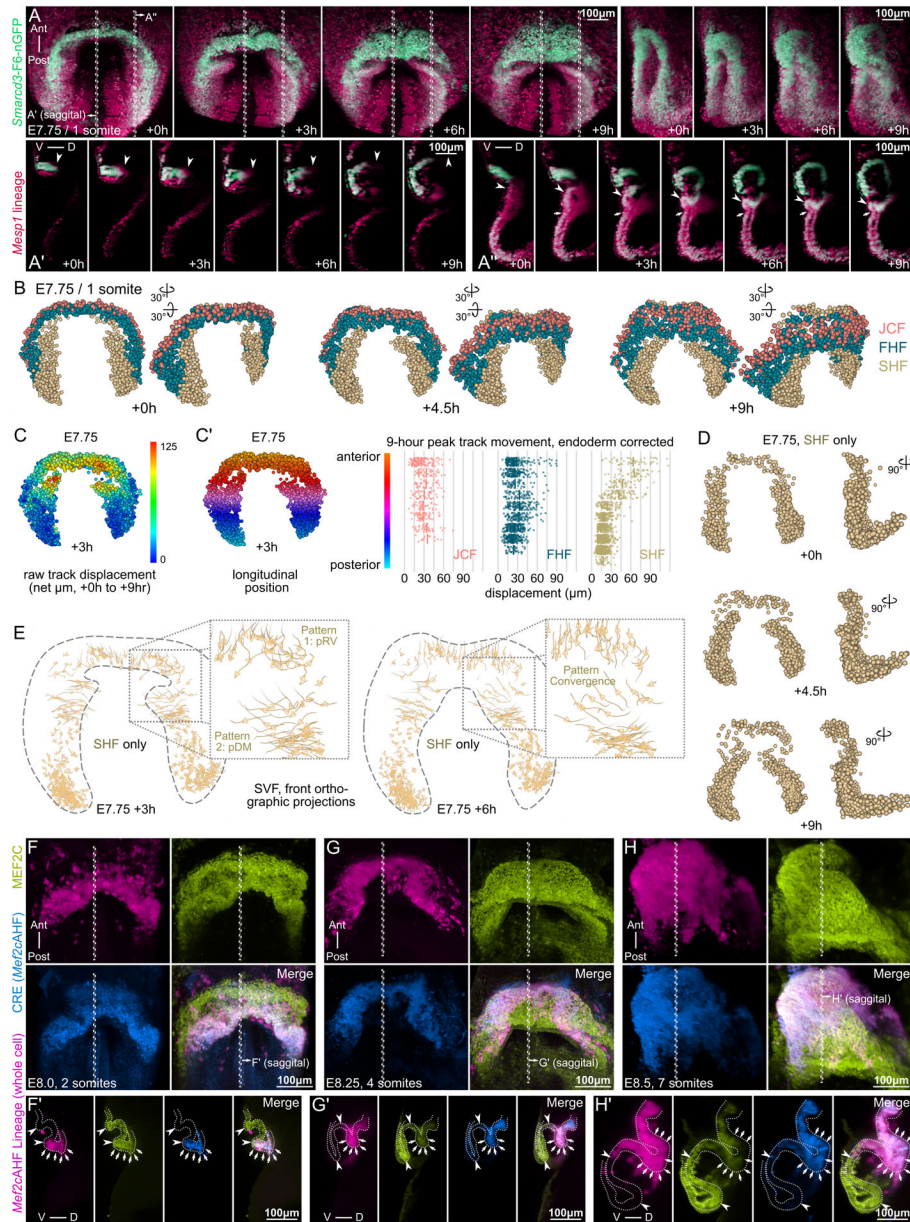
Figure 6: Transformation of the epithelial cardiac crescent into the early heart tube

A-A". Time-lapse whole-embryo LSFM imaging starting at E7.75, with ventral max (left four panels in **A**) and lateral oblique (right four panels in **A**) projections. 7.5μm thick sagittal slices from indicated regions in **A** are also shown (**A'**, **A"**). Arrowheads and arrows in **A'** and **A"** point to congruent cells at different timepoints. **B**. SVF reconstructions of tracked images series are shown at indicated timepoints from ventral and angulated views, with only FHF, SHF, and JCF cells drawn. **C-C'**. Quantitative analysis of SVF reconstruction shown in **B**, with cells colored by their track's displacement (**C**) or by their anterior-posterior position (left panel in **C'**). **D**. SVF reconstructions were re-drawn from ventral and lateral views, with only SHF cells at indicated timepoints. **E**. Examination of morphogenic dynamics within the SVF revealing two distinct regional patterns. **F-H'**. LSFM examination of fixed embryos

for lineage tracing of *Mef2c*AHF, during LHT formation. Vental partial max projection views labeled for MEF2C protein, *Mef2c*AHF-Cre, and *Mef2c*AHF lineage are shown at 2 somites (**F**), 4 somites (**G**), and 7 somites (**H**). Midline sagittal planes (7.5μm thick slices) at indicated stages (**F'**, **G'**, **H'**) are examined for movement of SHF cells into the heart, a process that leads to dorsal mesocardium formation and closure of the LHT.
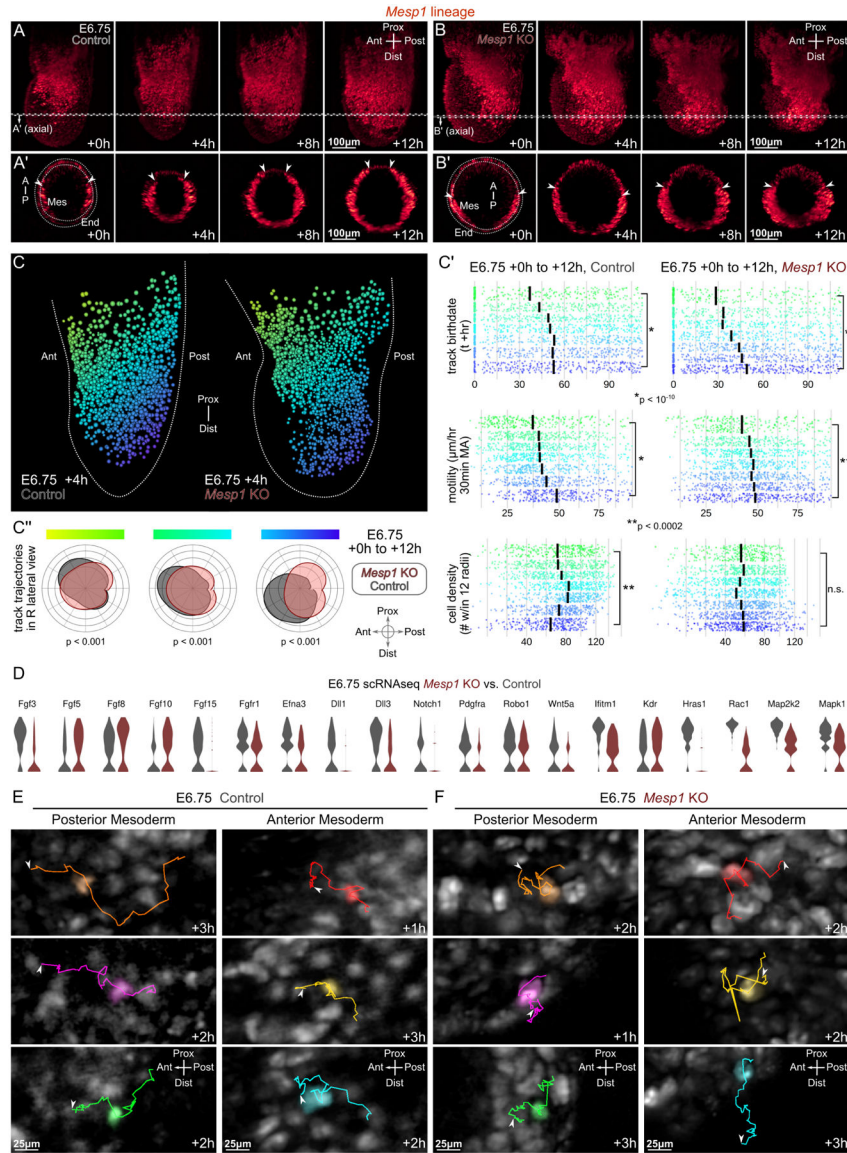
Figure 7: Loss of *Mesp1* disrupts the density gradient that forms following gastrulation, altering mesoderm organization

A-B'. Time-lapse whole-embryo LSFM imaging at E6.75. Control embryos: **A-A'**; *Mesp1* mutant embryos: **B-B'**. Max projection views are shown in lateral view left-half max projections. 7.5μm-thick axial cutaways from indicated regions in **A** and **B** are also shown (**A'**, **B'**). Mes = mesoderm, End = endoderm, A/Ant = anterior, P/Post = posterior, Prox = proximal, Dist = distal. **C-C'**. Quantitative analysis of raw TGMM tracks in control (left panels in **C-C'**) and *Mesp1* mutant (right panels in **C-C'**) time lapse data. C". Density distribution of mesoderm track trajectories. **D**. Single cell RNA sequencing of gastrulating mesoderm progenitors, with various migration-related features depicted by expression. **E-F**. Qualitative analysis of tracks (of duration 4–6h shown) in control (**E**) and *Mesp1* mutant (**F**) time lapse series. Left panel column in each of **E** and **F** show TGMM tracks originating in posterior regions, where right panels in each show anterior originating tracks. Arrowheads

in **E** and **F** demarcate track endpoints. Nuclei orientation p-values are from Watson's U_2 test (C").

Key resources table

REAGENT or RESOURCE	SOURCE	IDENTIFIER
Antibodies		
tdTomato (rabbit polyclonal)	Rockland	600-401-379
multi-RFP 5F8 (rat monoclonal)	Allele Biotechnology	ACT-CM-MRRFP10
Cre (rabbit polyclonal)	Millipore	69050
GFP (chicken polyclonal)	Aves	GFP-1020
Foxc2 (sheep polyclonal)	R&D	AF6989
Nkx2.5 (goat polyclonal)	Santa Cruz	sc-8697X
Isl1 (rabbit polyclonal)	Abcam	ab-109517
Mef2c (sheep polyclonal)	R&D	AF6786
Cd31 (hamster monoclonal)	Bio-Rad	MCA1370Z
Tnnt2 Ab-1 (mouse monoclonal)	ThermoFisher	MS-295-P
Hcn4 (rabbit polyclonal)	Alome	APC-052
Msx1 (goat polyclonal)	R&D	AF5045
pHH3 HTA28 (rat monoclonal)	Biolegend	641002
Cdh2 (mouse monoclonal)	ThermoFisher	33–3900
Ctnna1 (mouse monoclonal)	ThermoFisher	13–9700
Snai1 (rabbit monoclonal)	Cell Signaling Technology	3879
Jup (γ-catenin; rabbit polyclonal)	Cell Signaling Technology	2309
Pan-cadherin (rabbit polyclonal)	Cell Signaling Technology	4068
Fab fragment donkey anti-mouse	Jackson Immunoresearch	715-007-003
Dy405, AF488, Cy3, AF647, AF680 Secondary antibodies (donkey polyclonal whole IgG)	Jackson Immunoresearch	various
Chemicals, peptides, and recombinant proteins		
Low MP agarose	Fisher	BP165–25
Gelatin	Sigma	G1890
Rat Serum, special collection	Valley Biomedical	AS3061-SC
Fetal bovine serum	ThermoFisher	10082139
DMEM/F-12	ThermoFisher	11039021
GlutaMAX	ThermoFisher	35050061
ITS-X	ThermoFisher	51500056
Penicillin/Streptomycin	ThermoFisher	15070063
b-estradiol	Sigma	E8875
Progesterone	Sigma	P3972
N-acetyl cysteine	Sigma	A7250
CB-DMB	Sigma	C5374
EasyIndex OCS (R.I.=1.46)	LifeCanvas	EI-Z1001
Glass capillary and piston, largest	Sigma	Z328510 and BR701934
Glass capillary and piston, large	Sigma	Z328502 and BR701938

REAGENT or RESOURCE	SOURCE	IDENTIFIER
Glass capillary and piston, small	Sigma	Z328480 and BR701932
Glass capillary and piston, smallest	Sigma	Z328472 and BR701930
PFA 16%	Electron Microscopy Sciences	15710
Triton X-100 "TX-100"	Sigma	X100–500ML
SDS 20%	Research Products International	L23100–500.0
Wide orifice low-retention tips	Rainin	30389197
PVA with DABCO	Sigma	10981
Deposited data		
Fused live embryo repository	This paper	https://idr.openmicroscopy.org, accession 'idr0146'
- embryo1: E6.5 / MS, Mesp1 lineage	This paper	embryo1/
- embryo2: E6.75 / LS, Mesp1 lineage	This paper	embryo2/
- embryo3: E6.75 / LS Mesp1 KO, Mesp1 lineage	This paper	embryo3/
- embryo4: E7.0 / EB, F6/Mesp1 lineage	This paper	embryo4/
- embryo5: E7.0 – E7.25 / LB, F6/Mesp1 lineage	This paper	embryo5/
- embryo6: E7.25 / EHF, F6/Mesp1 lineage	This paper	embryo6/
- embryo7: E7.25 – E7.5 / EHF, F6/Mesp1 lineage	This paper	embryo7/
- embryo8: E7.5 / EHF, / F6/Mesp1 lineage	This paper	embryo8/
- embryo9: E7.75 / 1som, F6/Mesp1 lineage	This paper	embryo9/
scRNAseq: E7.5-E8.0	Tyser et al., 2021[9]	https://content.cruk.cam.ac.uk/jmlab/mouseEmbryonicHeartAtlas/
scRNAseq: E7.75-E8.25	de Soysa et al., 2019[39]	GEO series: GSE126128
scRNAseq: E6.75 Mesp1 KO	Krup et al., 2022[49]	GEO series: GSE208153
bulk RNAseq: E8.75 Isl1 KO	Gao et al., 2019[43]	GEO series: GSE126406
microarray: ISL1 KO hESC diff.	Quaranta et al., 2018[42]	N/A
Experimental models: Organisms/strains		
Mouse: Mesp1-Cre	Saga et al., 1999[8]	N/A
Mouse: RCL-H2B-mCherry	Jackson Laboratory	cat: 023139
Mouse: Smarcd3-F6-nGFP	Devine et al., 2014[6]	N/A
Mouse: RCL-tdTomato (Ai14)	Jackson Laboratory	cat: 007914
Mouse: Smarcd3-F6-CreERT2	Devine et al., 2014[6]	N/A
Mouse: Mef2cAHF-Cre	Dodou et al., 2004[57]	N/A
Mouse: Isl1-Cre	Cai et al., 2003[12]	N/A
Mouse: Nkx2–5-flox	Jackson Laboratory	cat: 030554
Software and algorithms		
Seurat 4.0 (R 4.0)	Hao et al., 2021[64]	https://github.com/satijalab/seurat

REAGENT or RESOURCE	SOURCE	IDENTIFIER
ggplot2 (R 4.0)	Wickham, 2016[68]	https://github.com/tidyverse/ggplot2
TopGO 2.48.0 (R 4.0)	Alexa and Rahnenfuher, 2022[67]	https://git.bioconductor.org/packages/topGO
GOplot 1.0.2 (R 4.0)	Walter et al., 2015[69]	https://github.com/wencke/wencke.github.io
F-TGMM v2.5	This paper [Fig. 1 (e)] and Fernando Amat[29]	https://github.com/mhdominguez/F-TGMM
ZLAPS (ZEN lightsheet adaptive positioning system)	This paper [Fig. 1 (a)]	https://github.com/mhdominguez/ZLAPS
TGMM2SVF	This paper [Fig. 1 (g)] and Leo Guignard[29]	https://github.com/mhdominguez/SVF
SVF2MaMuT	This paper [Fig 1 (g)] and Leo Guignard[29]	https://github.com/mhdominguez/SVF2MaMuT
Fiji (base ImageJ v1.53f)	Schindelin et al., 2012[34]	https://github.com/fiji/fiji
- PSF Generator	Biomedical Imaging Group at EPFL	http://bigwww.epfl.ch/algorithms/psfgenerator/
- Parallel Spectral Deconvolution	Piotr Wendykier	https://sites.google.com/site/piotrwendykier/software/deconvolution/parallelspectraldeconvolution
- CZI LSFM Processing Scripts	This paper [Fig. 1 (b) and (d)]	https://github.com/mhdominguez/LSFMProcessing
- BigStitcher	This paper [Fig. 1 (c)] and Preibisch Lab[28]	https://github.com/mhdominguez/multiview-reconstruction
- KLB file format	McDole et al., 2018[29]	https://github.com/JaneliaSciComp/keller-lab-block-filetype/
- MaMuT	This paper [Fig. 1 (f)] and Wolff et al.[30]	https://github.com/mhdominguez/MaMuT
MaMuT script library	This paper [Fig. 1 (h)]	https://github.com/mhdominguez/MaMuTLibrary